WATER – SOLID INTERFACES OF TEXTURED MATERIALS

A Dissertation

by

HYUNHO CHOI

Submitted to the Office of Graduate and Professional Studies of
Texas A&M University
in partial fulfillment of the requirements for the degree of

DOCTOR OF PHILOSOPHY

Chair of Committee,	Hong Liang
Committee Members,	Xinghang Zhang
	Jun Zou
	Partha P. Mukherjee
Head of Department,	Andreas A. Polycarpou

August 2016

Major Subject: Mechanical Engineering

Copyright 2016 Hyunho Choi

ABSTRACT

The water-material interface is of fundamental importance in nature and in wide engineering applications. Behaviors such as wettability, adhesion and penetration are influenced by the surface morphology. There is growing need in textured surface leading to increased interests in understanding the surface properties of textured materials. To date, the existing wetting models are limited to well-defined surfaces. The adhesion mechanism between water and textured surfaces is not well-understood. Moreover, stability and kinetic behavior of a water drop on a porous surface has yet to be understood. The objectives of this research are:

1) Revealing the principles behind a water drop and a porous surface;

2) Obtaining understanding about wetting, adhesion and penetration of a water drop; and

3) Identifying key parameters related to wetting for materials design.

In this research, the investigation about water-solid interface of textured materials is divided to three parts: wettability and adhesion; stability of penetration; and kinetic behavior of penetration. To examine wettability and adhesion on textured surface, super-hydrophobic surfaces of micro-beads/nano-pores were studied. It is for the first time to consider the synergetic effect of wetting and adhesion in textured surfaces. Next, the stability of a drop was studied to understand the penetration mechanism on hydrophobic porous surfaces. An experimental method combined theoretical approach was used through force balance principles. Results show that a

critical condition for spontaneous penetration on a porous surface, which is related to pore size, drop volume and surface wettability. During penetration, the kinetic behavior of a water drop has been investigated to reveal new principles such as the maximum penetrating rate, receding contact angle, slip-stick motion of contact circle. Results have revealed fundamental mechanisms of wettability, adhesion and penetration in water-textured material interfaces. Specific geometric design factors of textured materials, which are related to behaviors in water-solid interface, have been identified. The findings in this research lead to new approaches to optimize various applications of textured surfaces.

DEDICATION

This dissertation is dedicated to my beloved and supportive wife, Jeonga Lee, our sweet princesses, Yulli and Hailey, and to my always encouraging, ever faithful parent and parents-in-law.

ACKNOWLEDGEMENTS

First, I would like to thank my advisor, Dr. Hong Liang for her dedicated help, guidance, encouragement and precious advices for all through my PhD courses. I am thankful to my committee members; Dr. Xinghang Zhang, Dr. Jun Zou and Dr. Partha Mukherjee for their valuable suggestion to my research.

Thanks also go to my friends and colleagues in Surface Science Group for their precious time for discussion in my study and research. Specially, I wish to thank Dr. Sunghan Kim and Kyungjun Lee for their friendships and assistance.

NOMENCLATURE

Acronyms

CA	Contact angle
DI	Deionized
MP	Maximum penetration
PDMS	Polydimethylsiloxane
PVDF	Poly(vinylidene fluoride)
RCA	Receding contact angle
WA	Wetting angle
WCA	Water contact angle
YCA	Young's contact angle
ZrO_2	Zirconium dioxide

Symbols

η	Viscosity of water
γ	Surface tension of water
γ_{SV}	Surface tension of solid-vapor
γ_{LV}	Surface tension of liquid-vapor
γ_{SL}	Surface tension of solid-liquid
ρ	Density of water
θ	Contact angle
θ_a	Advancing contact angle (ACA)

θ_{CB}	Cassie-Baxter's contact angle
θ_d	Contact angle of a drop on pored surface
θ_m	Meniscus angle
θ_s	Roll-off angle (or sliding angle)
θ_r	Receding contact angle (RCA)
θ_W	Wenzel's contact angle
θ_Y	Young's contact angle
A	Surface area
d	Diameter of a pore
f_{A-L}	Ratio of total area of air-liquid interface
f_{S-L}	Ratio of total area of solid-liquid interface
F_D	Force of Laplace pressure
F_G	Gravitational force
F_M	Force by capillary pressure
F_{net}	Net force
F_{net}^S	Net force of a water drop on a single pore
F_{net}^M	Net force of a water drop on multiple pores
g	Gravitational acceleration
$h\ or\ l$	Penetration length
Δp	Pressure difference
r_s	Roughness factor
r_p	Pore radius

r_t	Outside radius of tube
R_x, R_y	Radii of curvature
R_c	Contact radius between a drop and surface
R_d	Radius of a drop on a pored surface
t	Penetration time
V_0	Initial volume of a drop
V_d	Drop volume
W_{SL}	Work of adhesion (Solid and Liquid)

TABLE OF CONTENTS

Page

LIST OF FIGURES

Page

LIST OF TABLES

Page

CHAPTER I

INTRODUCTION

This chapter provides information necessary to understand the background of the research regarding water-solid interfaces. It covers basic knowledges in wetting, adhesion, and penetration of textured materials having pores and surface morphology.

1.1. Liquid-solid interface

Interfaces are the boundary regions that separate two different phases of matter, such as liquid and insoluble solid, liquid and insoluble gas, and two immiscible liquids. They have special chemical, physical, and biological properties that have fascinated the attention of scientists and researchers in many fields [1, 2]. Among them, liquid-solid interfaces are fundamental in nature and useful in many application such as surface wetting [3], chemical processes [4], catalysis [5], electrochemistry [6], corrosion [7], lubrication [8], environmental science, materials science, and biological systems, among others [9, 10].

Since all natural materials including living plants and animals live with water and utilize it, water-solid interface is of fundamental importance in various natural phenomena ranging from wetting, adhesion, penetration, evaporation, and others. They show attractive behaviors such as super-hydrophobicity, self-cleaning, high adhesive surface, wicking, imbibition and others [9, 11-13] in Table 1.1 and 1.2. These behaviors in water-solid interface have strong relations with surface properties and structure of

materials. Many researchers have paid attention to the natural materials, and they have obtained lots of inspiration and ideas to develop novel materials. For examples, mimicking from super-hydrophobic surface of lotus leaf, waterproof coating method was developed based on micro/nano hierarchical structures and chemical modification [14, 15]. However, some behaviors in water-solid interface still remain questionable despite the numerous studies. What kind of textured surface can have high water-repellency? How can a water drop have high adhesion on water-repellent surface of rose petal? Which condition makes a water drop to go into a pore? How fast does a water drop penetrate into a pore? In order to answer these questions, understanding the effect of textured materials is needed. To control their behaviors, we need to reveal the principles behind a water drop - textured materials and then identify key parameters for materials design.

1.1.1. Textured materials

In nature, all materials have their own textures, which have regular, irregular, complex structures or patterns. Some textures are composed of micro- and/or nano-sized structures. Some textured materials have porous or fibrous or layered structures. These textured surfaces have interfaces with liquid and/or air having heterogeneity of pore space. As mentioned earlier, these textures on surfaces have interactions such as wetting, adhesion, penetration, and others, in water-solid interfaces. Specially, in the interface of water-porous surface, water can be absorbed or penetrated by capillary pressure depending on surface properties and morphology. For examples in nature, tree frog can

cling to smooth surfaces using sticky toe pads, which are composed of hexagonal blocks having small channels. Its strong adhesion is due to viscosity and also capillary forces generated by the fluid-filled channels [16]. Rock and soil are mainly composed of lots of grains and pores, so that they can absorb lots of water or oil [17, 18]. Their wetting and adhesion are related to pore size and porosity as well as surface properties of grains. They also affect the permeability, drainage and penetration of water. In water-solid interfaces, their behaviors such as wetting, adhesion and penetration are dependent on geometric factors of materials and surface properties. Understanding texture materials helps to design the novel materials for application in water-solid interface.

1.1.2. Wettability and adhesion in super-hydrophobic surfaces

In water-solid interface, wetting is one of the most attractive phenomena. Many researchers have paid much attention to super-hydrophobic surfaces in nature, because of their high water-repellency as well as other interesting properties such as self-cleaning, anti-corrosion, anti-contamination, and anti-icing [19, 20]. Super-hydrophobic surfaces such as lotus leaf,[1] cicada's wing,[2] water strider's leg,[3] and desert beetle's back [21, 22] have inspired many researchers to develop novel materials [23]. Their behaviors between natural materials and water are closely related to surface morphology [24]. In addition, a super-hydrophobic surface such as Lotus leaf has low adhesion due to micro/nano-sized hierarchical structures on a surface with low surface energy materials similar to wax [15]. In contrast, a water drop on rose petal and peanut leaf is attached on their hydrophobic surfaces [11, 14]. Their surfaces show high water-

adhesion regardless of high water-repellency because of their wrinkles and oriented structures on their surfaces [25]. Interestingly, the mechanism of wetting and adhesion of a water drop on super-hydrophobic surfaces is still not well-understood [26]. Also, existing wetting models such as Wenzel's, Cassie-Baxter's and others are limited to well-defined textured surface. Why do these super-hydrophobic surfaces have different adhesion? Generally, water-repellency and adhesion are conflicting concepts according to Dupre's equation [27]. Since liquid-solid work of adhesion is determined by $W_{SL} = \gamma_{LV}(cos\theta + 1)$, the contact angle is a critical factor. A high contact angle over 150° on a super-hydrophobic surface decreases the work of water-adhesion toward zero. Therefore, new understanding of wettability and adhesion mechanism in water-solid interface is needed.

1.1.3. Water penetration

Penetration is the action or process of making a fluid through or into something, which is a common behavior of fluid in porous media. In a number of processes in nature and our daily life, the fluid flow into porous materials is important. Examples are the capillary action of plants, oil penetration into limestone rocks, and soil being wet by the rain. Industrial applications such as micro-pipetting, ink-jet printing [19], textile manufacturing [20, 21], paper wicking [22], micro-fluidic devices [23, 24] and oil recovery [25, 26], involve the penetration of a liquid drop into capillary systems [27].

Until now, lots of studies have been conducted based on Lucas-Washburn's theory [28, 29]. The penetration into a porous surface depends on surface properties such as

porosity, pore size, the orientation of pores, and surface chemistry [29]. Basically, the driving force of water penetration into porous media is generated by capillary pressure, which is related to contact angles, pore radius and surface tensions. Also, the volume or radius of a drop is closely related to capillary pressure (or Laplace pressure) for spontaneous penetration. The main resistance of penetration is viscous drag of flow through pores. However, penetration of a water drop on porous media has more interesting behaviors such as the change of meniscus, receding contact angle (or contact angle hysteresis) and stick-slip motion. Their behaviors have close relation to wetting, adhesion and geometric factors on water-solid contact area. By identifying important factors involved in penetration, we can design porous surfaces and materials for application. More behaviors related to penetration time, rate and length can be clarified as well as the effect of pore size, drop volume and initial contact area of pored surface.

Table 1.1 Natural materials having super-hydrophobicity with low/high adhesion

Super-hydrophobicity with low adhesion		**Super-hydrophobicity with high adhesion**	
Natural materials	**Properties**	**Natural materials**	**Properties**
Lotus leaf	Self-cleaning Low adhesion	Rose petal	High adhesion
Butterfly wing	Self-cleaning Structural color	Peanut leaf	High adhesion
Fly eye	Anti-reflection Anti-fogging	Rice leaf	Anisotropic wettability
Peacock feather	Structural color	Spider capture silk	Water collection Mechanical property
Fish scale	Drag reduction	Gecko foot	High adhesion (S-S) Reversible adhesion Self-cleaning
Shark skin	Drag reduction Anti-biofouling		

Table 1.2 Adhesion mechanisms of natural materials

Natural materials	**Adhesion type**
Gecko	Van de Waals
Tree frog Sucker-footed bat (Myzopoda aurita)	Capillary adhesion
Disk-winged bat (Thyroptera tricolor) Octopus (Octopus vulgaris)	Sucker adhesion (Negative pressure of Boyle's law)

1.2. Fundamentals

1.2.1. Surface tension and capillary pressure

A liquid interface, or a liquid-vapor interface wants to contract in order to minimize surface area (or interfacial area) and its free energy. This tendency of these interfaces can be quantified in terms of surface tension or interfacial tension [30]. Sometimes, surface tension can be interpreted in terms of intermolecular forces. In equilibrium, when the curvature of meniscus is concave or convex, there is pressure difference between the two phases. As shown in Figure 1.1, the Young-Laplace Equation describes the relation between pressure difference and the curvature of meniscus by the following equation [31, 32],

$$\Delta p = \gamma_L \left(\frac{1}{R_x} + \frac{1}{R_y} \right) \tag{1. 1}$$

where R_x and R_y are the principal radii of curvature. As long as the pressures on both sides of the interface are equal, its boundary will stay planar. But, if the inside pressure is different from the outside pressure, a curved surface is formed. The pressure difference, Δp, is called the Laplace pressure.

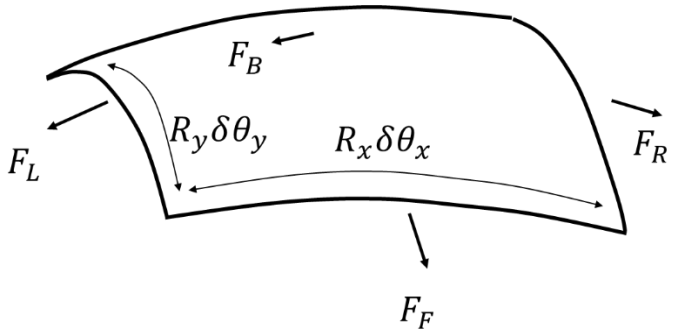

Figure 1.1 Surface tensions (forces) acting on a tiny curvature of surface. Surface tensions lead pressure by Young–Laplace equation

1.2.2. Wettability

Wettability is the ability of liquid to contact in a solid surface. Wettability is a fundamental surface property, which can be characterized by surface morphology and surface energy. When a liquid drop is deposited on a homogenous and flat solid surface, its wettability (or wetting) is determined by contact angle (θ_Y) according to Young's equation [31, 33]. Here, γ is the surface energy (or surface tension).

$$\gamma_{SV} = \gamma_{SL} + \gamma_{LV}\cos\theta_Y \quad (1.2)$$

On a real surface, there is some roughness on the surface. In a porous surface, surface roughness induced by heterogeneities of pores affects its wettability. As shown in Figure 1.2, in water-solid interface, the effect of surface roughness on wettability was explained by Wenzel's model [34] and Cassie-Baxter's model [35] and. Wenzel's model explains that surface roughness increases the area of water-solid surface. On a hydrophilic rough surface, a water drop has a tendency to spread out by developing more water-solid contact. In contrast, a water drop spreads less on a hydrophobic rough surface by

decreasing the liquid-solid contact area thermodynamically. The relation between the apparent contact angle (θ_W) on a rough surface and Young's contact angle (θ_Y) is explained by Wenzel's model as,

$$\cos\theta_W = r_S \cos\theta_Y \tag{1. 3}$$

Here, r_S is surface roughness factor, which is defined as the ratio of the actual surface area to its horizontal projection. In the Wenzel's model, intrinsically, surface roughness makes a hydrophilic surface more hydrophilic and also a hydrophobic surface more hydrophobic. In Cassie-Baxter's model, air is trapped having air-bags, which are formed between water and surface textures. Water forms a drop in contact on the heterogeneous surface of air and solid. Different surface area and energy change the wettability of water on a surface. The following Cassie-Baxter equation accounts for the change in apparent contact angle with heterogeneous surfaces.

$$\cos\theta_{CB} = r_f f \cos\theta_Y + f - 1 \tag{1. 4}$$

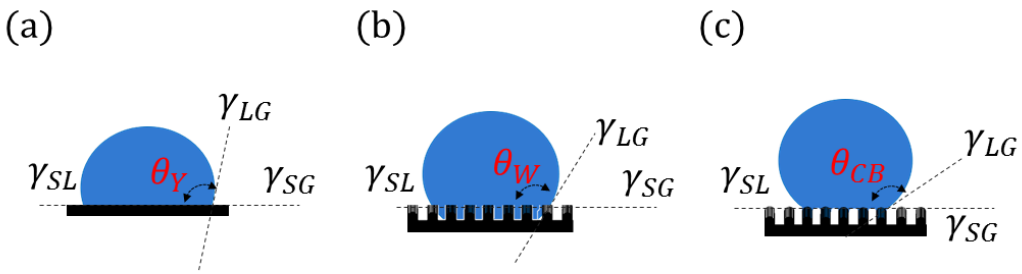

Figure 1.2 Schematics of contact angle: (a) Young's contact angle, (b) Wenzel's contact angle, and (c) Cassie-Baxter's contact angle.

In addition to the static contact angle, there are two dynamic contact angles such as advancing contact angle (ACA) and receding contact angle (RCA). As shown in Figure 1.3, these two contact angles are typically measured by two methods: 1) tilting plate method and 2) dynamic sessile drop method (or volume changing method). The tilting plate method is similar to the contact angle measurement in a static state. But the solid surface is being inclined from 0° to 90°. Contact angles are measured on both left and right sides of a sessile drop. These two contact angles are referred to advancing contact angle (ACA) and receding contact angle (RCA), and its difference is referred as to contact angle hysteresis (CAH). During this measurement, the water drop can roll off on a certain tiling angle, which is named roll-off angle (or sliding angle, θ_s) [36]. The dynamic sessile drop method is similar to the static sessile drop method, but it uses volume changing method. During adding volume of a drop continuously, the maximum contact angle is determined possible without the increase of its liquid-solid interfacial area. That is advancing contact angle (ACA). Volume is removed to form the smallest possible contact angle without the decrease of its interfacial area. The minimum is receding contact angle (RCA). The difference between the advancing and receding angle is contact angle hysteresis. [37]. This hysteresis is important for characterizing adhesion as well as surface wettability. Sometimes, the minimum roll-off angle by tiling the substrate is used to describe the contact angle hysteresis.

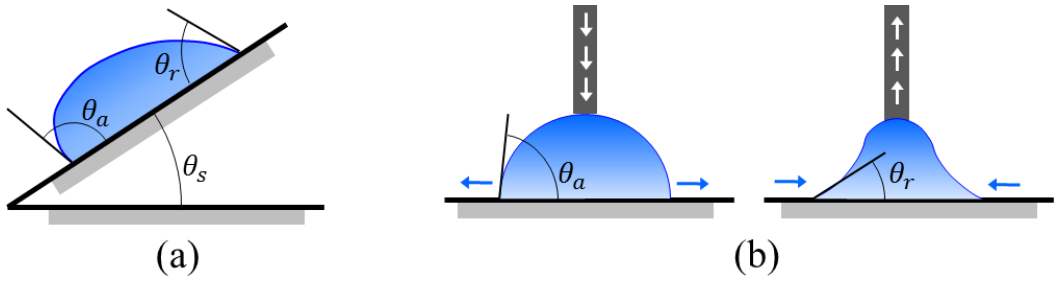

Figure 1.3 Schematics of dynamic contact angle measurement: (a) tilting plate method and (b) dynamic sessile drop method (or volume changing method)

1.2.3. Adhesion

Adhesion is the tendency of different materials or surfaces to attract each other. Based on interface and mechanism, there are various kinds of adhesion; 1) solid-solid, liquid-solid, and solid-liquid-solid and 2) mechanical, chemical, dispersive, diffusive adhesion, etc. However, there is no mechanism to estimate water adhesion in a water-solid interface. Usually, adhesion is related to other factors such as wettability, microstructure, capillary and so on [38]. Commonly, Dupre's equation explains liquid-solid work of adhesion based on surface energy and contact angle [27]. However, as mentioned in wettability, experimental methods to measure roll-off angle (or sliding angle) and contact angle hysteresis are usually used [37, 39]. Some researchers suggested experimental methods to measure adhesive force of a water drop by using a high-sensitive microelectromechanical balance system [40]. Specially, there is no reliable theoretical model to predict water-adhesion on a textured surface. Wetting and adhesion are inseparable in water-material interface and also they are closely related to

surface properties and surface morphology. Understanding wetting and adhesion of textured materials is critical for the design of novel materials.

1.2.4. Penetration

Fluid penetration into porous material is driven by capillary pressure. Since porous materials have complex structures, simplified porous samples is assumed. In Figure 1.4, when it has vertical parallel cylindrical pores randomly distributed, its capillary pressure which drives fluid into a pore is expressed by the Young-Laplace equation as

$$\Delta P = \frac{2\gamma \cos\theta_m}{r_p} \tag{1. 5}$$

Where ΔP is capillary pressure, γ is the surface tension of fluid, r_p is pore radius, and θ_m is contact angle (referred as to meniscus angle) formed between the fluid and the inner wall of the pore. But, when θ_m is over 90° in hydrophobic pore, its capillary pressure by the curvature of meniscus blocks the penetration.

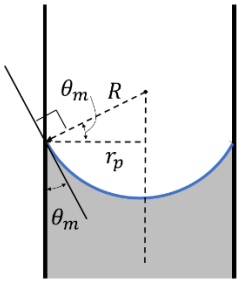

Figure 1.4 Schematic of spherical meniscus with contact angle less than 90° in a vertical tube

The study of penetration into a capillary tube was first reported by Lucas [28] and Washburn [29]. They considered a quasi-steady-state laminar flow of a Newtonian liquid in an infinite reservoir and a finite liquid drop [41]. Their work has been used as the basis for the understanding of liquid penetration into porous media [42]. Figure 1.5 shows the capillary uptake of water on a vertical tube. Neglecting gravitational and inertial effects, the penetration behavior of fluid from an infinite reservoir at a rate is assumed by the balance of capillary forces and viscous drag like this equation,

$$h(t) = \left(\frac{\gamma r_p \cos\theta_m}{2\mu} \right)^{1/2} t^{1/2} \qquad (1.\ 6)$$

Where h is the length that the fluid penetrates into a capillary, μ is viscosity, θ_m is contact angle between a meniscus and a capillary, and t is penetration time.

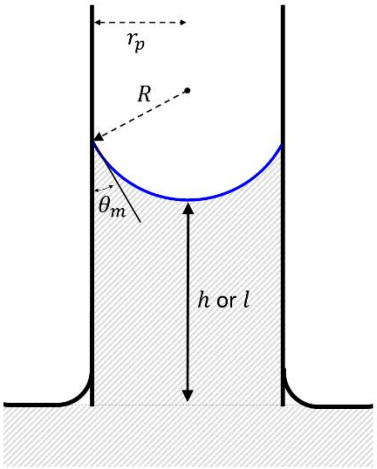

Figure 1.5 Schematic of capillary rise in a tube

The penetration of a small drop into a capillary tube was reported by Marmur [41, 43]. When a small drop contacts on a pored surface, it forms two curvatures of air-water interface: the curvature of a small drop outside the pore and the meniscus inside a pore. Penetration is driven by its pressure difference between two curvatures. A smaller and spherical drop with larger contact angle increases the pressure difference. Consequently, as the pressure difference is increased, the process of penetration is enhanced. Based on previous research [41-43], penetration of a water drop into a capillary can be described by the following equation, which can be used to verify the penetration behaviors.

$$\rho \frac{d}{dt}\left(l \frac{dl}{dt} \right) + \frac{8\mu}{r_p^{\,2}} l \frac{dl}{dt} = \frac{2\gamma}{R_d} + pg(1-\cos\theta_m) + \frac{2\gamma\cos\theta_m}{r_p} \qquad (1.7)$$

CHAPTER II

MOTIVATION AND OBJECTIVES

As discussed in Chapter I, the water-solid interface of materials is of fundamental importance in nature and in industry. Behaviors such as wettability, adhesion and penetration in water-material interface are largely dependent on the surface morphology. Though there are various wetting models to explain the effect of surface roughness, they are limited to well-defined surfaces. There is no clear adhesion mechanism between water and porous surfaces. In addition, stability and kinetic behavior of a water drop on porous surfaces still remains puzzling. Furthermore, critical factors to design porous materials are still not well understood. Geometrical factors need to be considered to functionalize their behaviors and optimize the structures.

The objectives of this research are: 1) Revealing the principles behind a water drop and a porous surface; 2) Obtaining understanding about wetting, adhesion and penetration of a water drop; 3) Identifying key parameters for materials design. To achieve these objectives, the research is followed through this flow shown in Figure 2.1. Behaviors in water-textured interface are divided to three parts: wettability and adhesion; stability of penetration; and kinetic behavior of penetration.

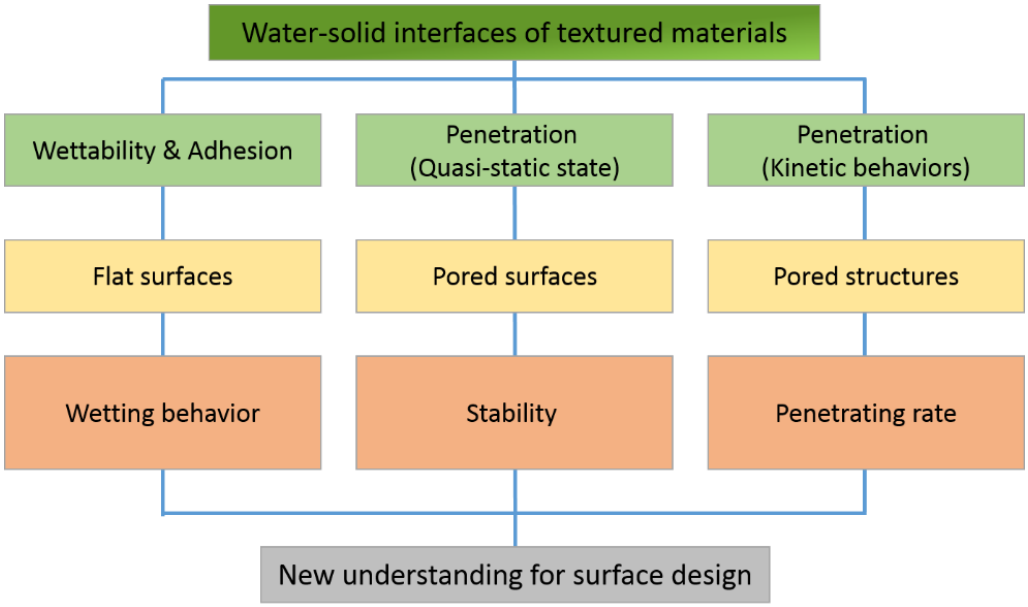

Figure 2.1 Research flow chart

The following discusses details of each of three activities shown in Figure 2.1.

1) New wettability and adhesion model in water-textured surfaces

Effect of textured surfaces on wettability and adhesion was studied in this research. As a texture surface, super-hydrophobic surface having micro-beads/nano-pores were fabricated by using new method combining spraying method and phase separation. This study can determine the role of micro-beads and nano-pores to control behaviors. Since wettability on a rough surface is dependent on surface heterogeneities, its porous surface can also show similar effect on wettability and its geometrical factors will influence its surface properties. Adhesion of a water drop on porous surface was studied based on experimental method. New adhesion mechanism between water and porous surface was suggested.

2) Stability of a water drop on porous surfaces

The stability of a drop was considered to understand the penetration mechanism on hydrophobic porous surfaces by experimental method and theoretical approach. When the surface is hydrophilic, water can easily go into a pore due to capillary pressure. When the surface is hydrophobic, capillary pressure by pores has opposite way to interrupt the penetration. For this research, polydimethylsiloxane (PDMS) hydrophobic pored samples with different diameters and pore densities were prepared. This study defined the critical condition for spontaneous penetration of a water drop on hydrophobic porous surface, which is related to pore size, drop volume and surface wettability.

3) Kinetic study of spontaneous penetration

When a water drop goes into a hydrophobic pore, its kinetic behavior was investigated in detail. To reveal new principles such as the maximum penetrating rate, receding contact angle and slip-stick motion, all parameters such as contact angle, drop radius, contact radius and penetration length were analyzed over time. This study can show the effect of geometrical factors of pored samples on penetration rate and trend.

This research revealed fundamental mechanisms of wettability, adhesion and penetration in water-textured material interfaces. Specific geometric design factors of textured materials, which are related to behaviors in water-solid interface, were identified. The findings in this research afford new approach to optimize applications of textured surface.

CHAPTER III

DESIGN AND SYNTHESIS OF A SUPER-HYDROPHOBIC PVDF-BASED COMPOSITE*

The ability to design, control, and synthesize a material surface with super-hydrophobicity is of great interests in many engineering applications. Here we report a cost-effective process to fabricate Poly(vinylidene fluoride) (PVDF) / Zirconium(IV) oxide (ZrO_2) composites with super-hydrophobicity. This is achieved by combining an anti-solvent that induces phase separation, i.e., the precipitation of PVDF from the solution through a spray-on method on various liquids. The material surfaces possess wrinkled micron-sized beads which displayed super-hydrophobicity in water without any chemical treatment. The process developed in this research presented is a fast and simple approach in making hydrophobic surfaces.

3.1. Introduction

Super-hydrophobic surfaces are widely found in nature. Among those are lotus leaves, rose petals, butterfly wings, fish scales, and bird feathers to repel water. Due to their unique and attractive properties such as self-cleaning, anti-fogging, anti-icing, and stain resistance, researchers have made great efforts to produce biomimetic or bio-

* Part of this chapter reproduced with permission from "Design and Synthesis of a Superhydrophobic PVDF-Based Composite" by Hyunho Choi, et al., *Journal of Tribology*, 2016, 138, 022301-1 (Copyright © 2016 by *ASME*);

inspired super-hydrophobic surfaces [12, 44, 45]. In general, super-hydrophobic surfaces like the lotus leaf have a high water contact angle above 150° and a very low tilting angle less than 10° [46]. Since a water droplet can easily roll off, it has self-cleaning ability due to its low adhesion force [47]. Unlike the lotus leaf, some of the super-hydrophobic surfaces such as the rose petal have a high adhesion force so that water droplets can stay by pinning to the surface [46].

When a water droplet is placed on a flat solid surface, it forms a spherical shape having a contact angle (ɵ). This angle can be expressed by Young's equation related to surface tensions of liquid-air, solid-liquid and solid-air. But wetting in real surfaces is more complex due to surface texture and chemical difference. In rough solid surfaces, wetting basically shows two different wetting states; Wenzel state and Cassie state. In Wenzel state, when apparent contact angle (ɵ) on flat surface is under 90°, wetting is increased by roughness. And when ɵ is over 90°, wetting is decreased by surface roughness [48]. Cassie state shows wetting on heterogeneous surface. When air is be trapped between peaks of a rough surface and a water droplet forms air pockets., In this case this surface becomes repellent to the water due to air and wetting is decreased [35].

Fabricating a super-hydrophobic surface involves the consideration of two strategies: to roughen the surface and to modify the surface chemically by using low surface energy [49, 50]. Many reports have been found to introduce roughness for super-hydrophobicity. Examples are lithography [51], electro-spinning [52], electro-spraying [53], plasma etching [54], sol-gel processing [55], chemical deposition [56], phase separation [57] among others [58]. But some of these methods require expensive tools,

complicated setups, and/or multi-step processes [12]. Often the fabrication rate is too slow or area is too small [59]. Among them, an air-spraying method is a simple and fast method for coating and thin film production. Since an air spray gun forms atomization of solution, the spraying speed and flow rate can be easily controlled by air pressure and nozzle size. This method has been usually used to fabricate super-hydrophobic surfaces [60]. Polymer composites have also been used to fabricate super-hydrophobic surfaces. Adding inorganic materials introduces surface textures. [61-64]. Well-dispersed micro- or nano-particles in polymer matrix promote roughened surfaces [65]. In addition, they have been used for fabricating porous structures such as membrane for gas separation and filtration.

In this study, we used poly(vinylidene fluoride) (PVDF) and Zirconium oxide (ZrO_2) nanoparticles for fabricating super-hydrophobic surface. PVDF is a common thermoplastic fluoropolymer with low surface energy and low melting point (177°) [66]. It has many applications as a film, tubing, piping, insulator and membrane filters due to its chemical resistance and good mechanical property. ZrO_2 is an important inorganic material having chemical inertness, excellent mechanical properties and thermal stability. Dispersed ZrO_2 nanoparticles are attractive for fabrication of porous structures [67, 68].

PVDF is naturally water-repellent but PVDF flat films do not have a large water contact angle to be considered super-hydrophobic [65, 69]. And PVDF films fabricated by spraying on solid substrates did not have the necessary roughness for the surface to exhibit super-hydrophobicity. Sprayed droplets crumbled when they collided with the

solid substrate and their boundaries were collapsed due to the slow evaporation of solvent. To develop an effective method for the fabrication of super-hydrophobic surfaces with various textures, we sprayed the solution onto the surface of various liquid baths by using air-spray gun. We obtained PVDF/ZrO_2 composites having improved hydrophobicity and different adhesion forces. The water contact angle is larger than 150° and a tilting angle is 22° without any chemical treatment.

3.2. Experimental

This research is to design and develop a polymer based composite in order to have favorable surface structures. The matrix is poly(vinylidene fluoride) (PVDF, average Mw ~275,000) and enhancement is Zirconium(IV) oxide (ZrO_2) nanoparticles. PVDF was chosen because of its low surface energy and low melting point. ZrO_2 nanoparticles were selected based on their dispersion-ability on PVDF solution and ability to form porous structure [70]. PVDF and ZrO_2 were obtained from Sigma-Aldrich. Dimethyl sulfoxide (DMSO, from BDH) and acetone were used as solvents. Water and ethanol were used as anti-solvents.

To make the matrix, we dissolved 1 g PVDF pellets in 20 mL of a 50:50 solvent mixture of DMSO and acetone, and stirred them at 60 °C for 24 hours. To fabricate composites, 1 wt% of ZrO_2 of 100 nm size was added. The process steps are illustrated in Figure 3.1(a). As illustrated a commercial airbrush (Master Airbrush G444, 0.2 mm needle & nozzle) was used for spraying at a controlled air pressure of 20 psi. Prepared solution was sprayed for 15 minutes (15 mL/h) at 20 cm distance. Different substrates

were used to deposit the sprayed films: deionized (DI) water bath and ethanol/DI water bath. Formed films were floating on top of liquid baths. This resulted in white films (100 mm diameter), shown in Figure 3.1(b). Films were slightly washed by DI water to eliminate remaining DMSO/acetone and dried for 24 hours in 100 °C chamber.

After samples were prepared, to characterize the morphology of films, we used optical microscope (Keyence VHX-2000) and scanning electron microscopy (SEM, VEGA3-SB). Static contact angle and tilting angle (when the droplet started to slide or roll as the increase of tilting angle from 0°) were measured at six different locations of each sample using a home-made goniometer. The error bars were obtained based on the calculation through standard deviation of six repeated tests. he roughness of films was measured using a laser microscope (Keyence VK-9710).

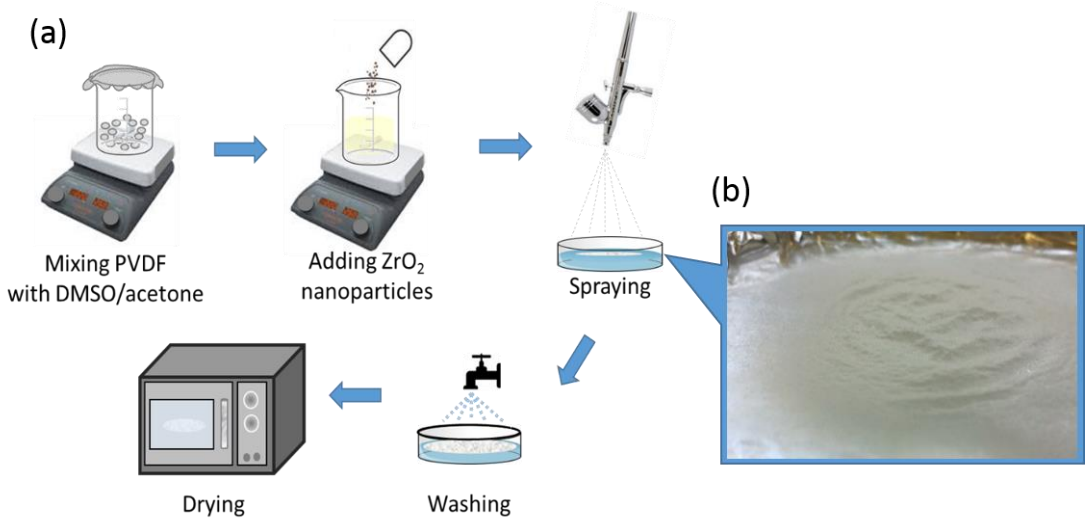

Figure 3.1 Schematic fabrication process of spraying method (a) and PVDF films sprayed on water bath (b).

3.3. Results and discussions

Samples were fabricated using a spraying method and phase separation method by water and ethanol/water. ZrO_2 nanoparticles were added in order to study their effects on super-hydrophobicity.

3.3.1. PVDF films

In order to understand the process-microstructure of the surface, SEM analysis was conducted and results are shown in Figure 3.2. The bottom of PVDF film contacted with water is composed of many spherical beads which diameters are 5 - 50 μm like Figure 3.2(a2). Some beads are flat and connected each other. This is because droplets of sprayed solution hit the water's surface and were precipitated having spherical shapes and porous structures on water. When micro-sized beads on the bottom are invested in detail, there are many pores up to 400 nm on surface. (Figure 3.2(a3)) On the other hand, the upper side of PVDF film to the air has networked texture consisting of fibers and beads shown in Figure 3.2(a1). When sprayed solution covered almost all of the water surface, they could not easily contact water and their precipitation became limited. Some droplets of sprayed solution were crumbled on formed film and their shapes became flatter. Some of the droplets moved along air flow which caused the sprayed solution to form fibers. According to this concept of deposition process, both sides of film had different textures.

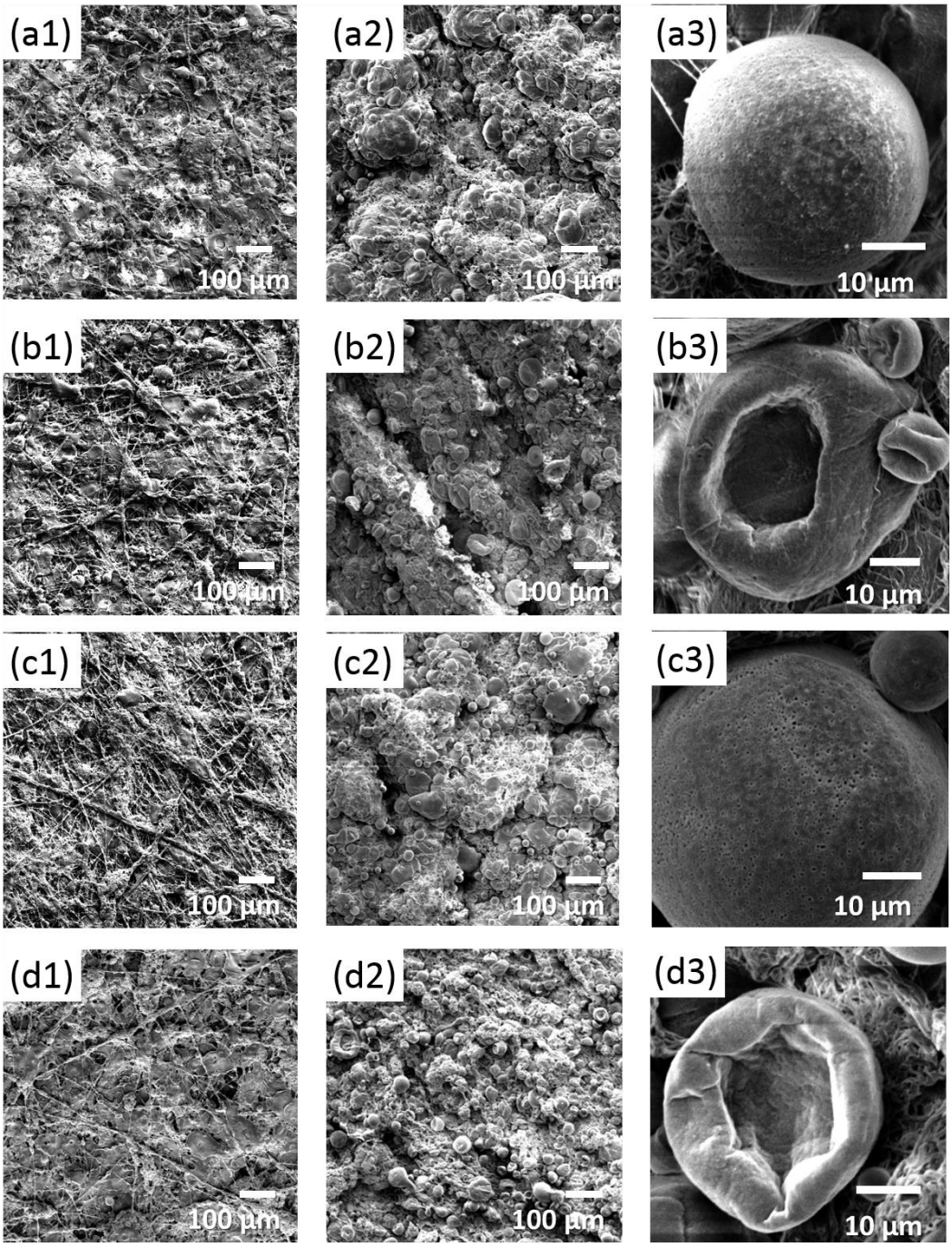

Figure 3.2 SEM images of (1) upper sides, (2) bottom sides and (3) beads on bottom: PVDF film (a) on water, (b) on ethanol/water, PVDF/ZrO_2 PVDF film (c) on water and (d) on ethanol/water

In this process, water played two roles; a shock absorber and a precipitator as anti-solvent. Water could reduce dropping impact of sprayed solution by air blow and avoid crumbling of their shapes. PVDF dissolved by solvents which boiling points are high such as DMSO (189 °C) could not be easily extracted by common evaporation. But PVDF could be easily and quickly precipitated while maintaining the shape of sprayed solution by using water due to phase separation [71]. During this process, some droplets of sprayed solution sometimes changed to flatter shapes on water by their aggregation and spreading out. Some of them had porous structures in part. Precipitated PVDF micro-beads had many nano-sized pores formed by fast polymer precipitation by water. According to the previous research, fast precipitation by water could form long finger-like pores and its depth and size are dependent on solvent, concentration, and film thickness [72].

Next, instead of DI water, ethanol/DI water mixture was used. Since PVDF solution was not precipitated when ethanol concentration is over 50% in water/ethanol mixture, the highest concentration (50%) of ethanol was used. As shown in Figure 3.2(b), the bottom of PVDF film formed on ethanol/water has more irregular beads and porous structures in part. Some beads have bowl-like shapes. The diameters of beads are 10 - 70 μm. As increase of spraying time, fibers and droplets accumulated on the upper side of PVDF film, PVDF film had networked texture same as a film on water. Initially sprayed solution made a film floating on ethanol/water but formed films looked like wet and gel-like. It was due to slow precipitation of PVDF by the presence of ethanol in bath [71, 72].

As shown in Figure 3.3, two types of PVDF films formed on water and ethanol/water have static water contact angles of 145 ±3° and 145 ±5°, which are higher than that of flat PVDF film. It is due to micro-sized beads on surface or air pockets between irregular beads. In tilting angle measurement, there was no sliding and no rolling behavior on networked-texture of the upper sides of all films. Water droplets (5, 10, 20 μL) could be attached on the surface at 90° and 180° of tilting angles. As shown in Figure 3.4, only the bottom of PVDF film formed on ethanol/water has rolling behavior by using 20 μL water droplet, and it ranges from 27° to 45°. But there was no rolling by smaller water droplet. Large ranges of contact angles and tilting angles are due to less uniformity of surface morphology and irregularity of micro beads.

3.3.2. PVDF/ZrO_2 composites

To obtain super-hydrophobic surface, PVDF was mixed with 1 wt% ZrO_2 nanoparticles in DMSO/acetone at 60°C for 24 hours. Prepared solution was sprayed by same procedure. The morphology of two PVDF/ZrO_2 composite films formed on water and ethanol/water are similar to those of PVDF films respectively. As shown in Figure 3.2(c1) and 3.2(d1), the upper sides of both films also have networked textures same as PVDF films but some droplets of PVDF/ZrO_2 composite film are more spread out. It is because droplets of sprayed solution floating on ethanol/water was crumbled before precipitation like crushed water balloon. These crumbled beads makes the surface less rough, its contact angle is smaller in Figure 3.3. On the bottom of PVDF/ZrO_2 composite film formed on water in Figure 3.2(c2), there are more beads which sizes are similar to

those of PVDF films. There is no big difference of contact angles between two films, but the size of pores on beads were as large as 600 nm which is larger than the pore size in the PVDF film.

PVDF/ZrO_2 composite film formed on ethanol/water has porous structures in part and more irregular beads having more wrinkles on the bottom. Some beads also have bowl-like shapes. These wrinkles and bowl-like shapes are helpful for being super-hydrophobic surface. PVDF/ZrO_2 film formed on ethanol/water has largest water contact angle as 150 ±4° and smallest tilting angle for rolling ranges from 21° to 36°. Its tilting angle is larger than those of super-hydrophobic surfaces having the lotus effect but this film shows super-hydrophobicity [73].

From SEM micrographs, mainly morphology of films is not affected by the presence of ZrO_2. ZrO_2 nanoparticles are not seen and they are hidden by PVDF. But previous research showed that weak interaction at the interface of PVDF and ZrO_2 particles could form many pores on films. [70] We assumes that ZrO_2 nanoparticles would be relatively related to sizes of pores and wrinkles and they were helpful to be more hydrophobic surface.

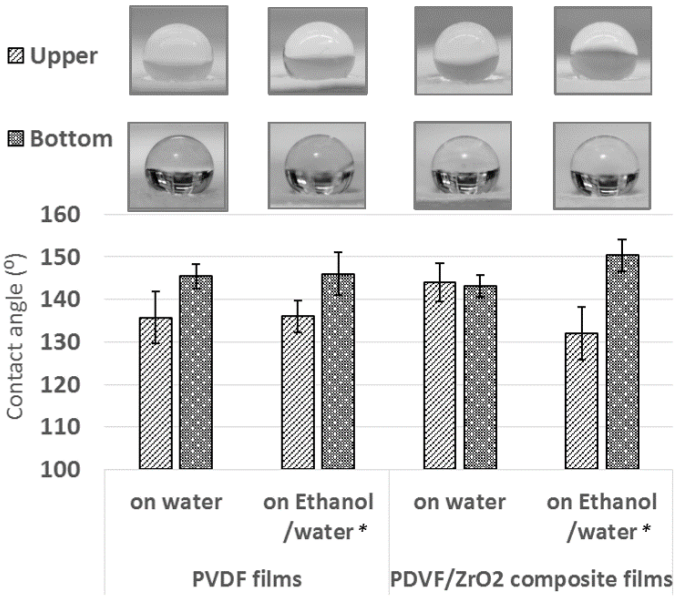

Figure 3.3 Static contact angle by 5 µL water droplets (* two-sample t-test, p = 0.0275)

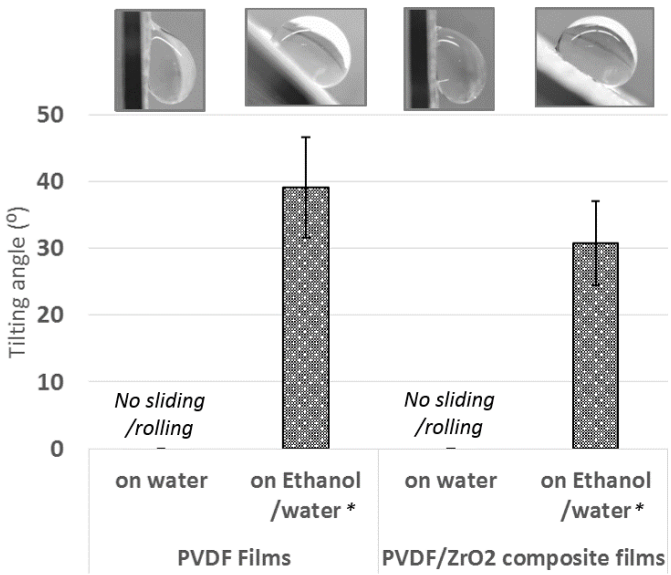

Figure 3.4 Tilting angles for sliding of 20 µL water droplets (* two-sample t-test, p = 0.0127)

3.3.3. Hydrophobicity

To estimate hydrophobicity of these films, surface profiles were measured. Due to the favorable hydrophobicity, only the bottom was conditioned for all samples. As shown in Figure 3.5, PVDF film formed on water have more monotonous surface profile than that on ethanol/water. Table 3.1 shows the surface roughness. Its surface profile as shown in Figure 3.5(a) shows sub-variation (around 7 μm). This is due to the small micro-beads and porous structures. PVDF composite film formed on ethanol/water had more irregular surface profile, as shown in Figure 3.5(b). It is due to irregular beads having many wrinkles which can be observed in the SEM image (Figure 3.2(d2). PVDF/ZrO_2 composite films had exhibited similar surface profiles. PVDF/ZrO_2 composite film on water had a less monotonous profile than PVDF film on water due to more spherical beads having nano-sized pores on surface. PVDF/ZrO_2 film on ethanol/water had the most fluctuated surface profile having even more sub-variation like Figure 3.5(d). In addition, water contact angles of all samples were found to decrease in the range of 3° ~ 10° after 10 minutes (data not shown). The water drop is slightly smaller. This indicates vaporization of the droplets and the surface did not show significant effects of roughness on the change of wetting angle in time.

Based on the results, there are two possible wetting models to illustrate the surface textures obtained on water and on ethanol/water, as shown in Figure 3.6. Here in Figure 3.6(a), the surface composes the spherical micro-sized beads that improved the hydrophobicity, as seen in the wetting angle data in Figure 3.3. This surface shows high adhesion toward a water droplet in Figure 3.4. It is believed that the nano-sized pores on

beads can make high adhesion of water droplet on surface due to capillary force [74]. The Figure 3.6(b) illustrates the surface extruded with irregular beads and bowl-like beads having many wrinkles that has been seen in the SEM image (Figure 3.2(d)). They are believed to be responsible for the super-hydrophobicity (Figure 3.3). This surface also shows lower adhesion force (Figure 3.4). These results agree with the previous reports that bowl-like bead can help for super-hydrophobicity [75].

Table 3.1 Roughness of bottom sides: PVDF films and PVDF/ZrO_2 PVDF composite films

	Rp (µm)	Rv (µm)	Rz (µm)	Ra (µm)	Rq (µm)
PVDF (Water)	201.51	252.53	454.04	25.02	29.68
PVDF (Ethanol/Water)	272.13	142.35	414.48	27.31	32.70
PVDF/ZrO_2 (Water)	272.80	347.09	618.89	37.20	45.56
PVDF/ZrO_2 (Ethanol/Water)	297.25	183.03	462.27	26.29	33.42

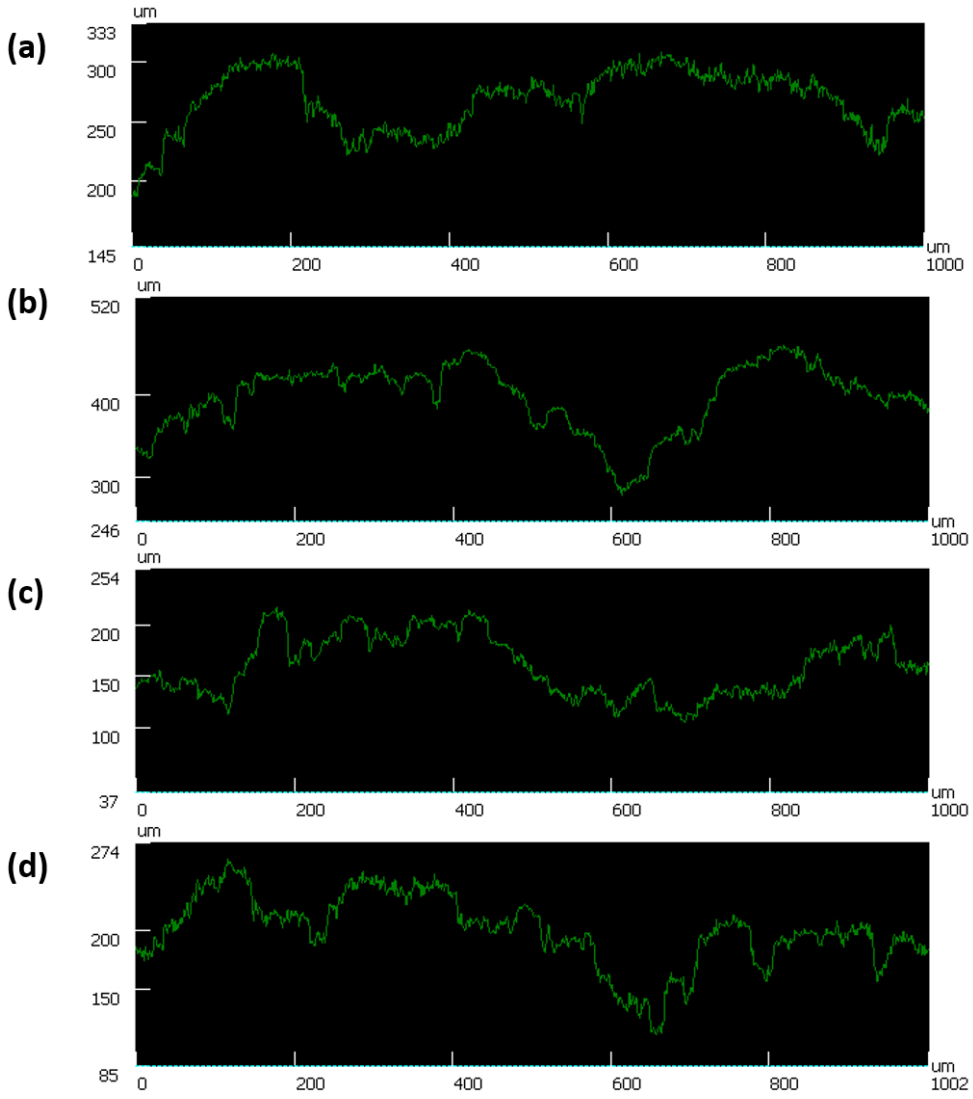

Figure 3.5 Surface profiles of bottom sides: PVDF film (a) on water, (b) on ethanol/water and PVDF/ZrO_2 composite PVDF film (c) on water, (d) on ethanol/water

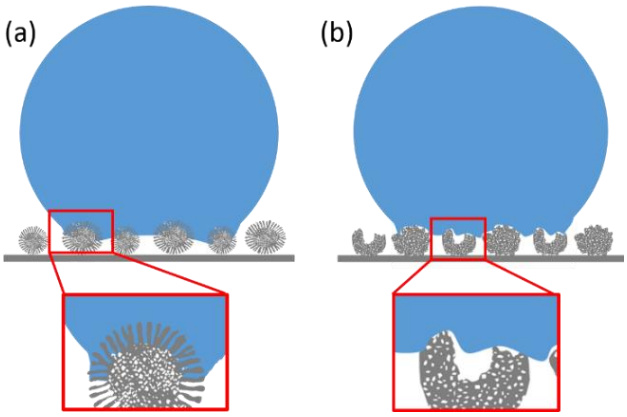

Figure 3.6 Schematics of wetting models of improved- or super-hydrophobic PVDF films and PVDF/ZrO_2 films (a) on water and (b) ethanol/water

3.4. Conclusions

We developed a spraying method using various liquids to generate super-hydrophobic surfaces of PVDF and PVDF/ZrO_2 composite films. Two groups of surfaces were fabricated: improved hydrophobic surface of PVDF and super-hydrophobic surface of the composite. PVDF and PVDF/ZrO_2 composite films were formed on water resulting in many spherical micro-beads with nano-sized pores. Micro-beads were found to improve the hydrophobicity with the contact angle around 143 ±3° and the adhesive force was to attach water droplet of 20 µL. The PVDF/ZrO_2 composite film formed on ethanol/water had irregular wrinkled micro-beads and bowl-like beads resulting super-hydrophobicity with the contact angle of 150 ±4°.

In the fabrication process, the roughness was introduced by precipitation of sprayed solution on water and ethanol/water. Water acted as an anti-solvent, which induced fast precipitation of PVDF from the solution. Ethanol is an important factor to change shapes

of beads in order to reduce the speed of precipitation. The surface morphology was altered due to a solvent and anti-solvent such as DMSO and ethanol/water. This simple and fast spraying method by various liquid can be extended to fabricate the super-hydrophobic surface having different adhesion forces. This method is scalable and can be used to make large-sized films up to meters at a fast rate.

CHAPTER IV

WETTABILITY AND SPONTANEOUS PENETRATION OF A WATER DROP INTO HYDROPHOBIC PORES[*]

The penetration of a water drop into hydrophobic pores reflects its instability on a porous surface. To understand the mechanism of penetration and to predict the behavior of such a drop, an investigation was conducted through experimental study combined theoretical analysis. Water drops with volumes from 0.5 to 15 μL were examined on Polydimethylsiloxane (PDMS) substrates containing pores of 800 μm and less in diameter. Results showed a critical condition at which a drop starts to penetrate into a certain sized pore. The critical condition presents a parabolic relationship between the volume of a water drop and the size of a hydrophobic pore. This behavior was due to a net force resulting from Laplace pressure, and capillary pressure. This force was found to be affected by the porosity, wetting angle, and there after the critical condition. The finding of this research will be beneficial for future design of structured surfaces.

4.1. Introduction

Liquid penetration of a drop into porous media occurs in nature and also in industry. It has been an attractive topic in a wide range of applications such as papers/textiles [76],

[*] Part of this chapter reproduced with permission from "Wettability and Spontaneous Penetration of a Water Drop into Hydrophobic Pores" by Hyunho Choi, et al., *Journal of Colloid and Interface Science*, 2016, 477 (1), 176-180 (Copyright © 2016 by Elsevier Inc.);

membranes [77], microplates/pipetting [78], ink-jet printing [79], oil recovery [80], micro-fluidics [81], and so on [82, 83]. Liquid penetration has been studied by many researchers such as Lucas [28], Washburn [29], Marmur [41], and others [84]. Capillary rise of a small drop in a hydrophobic tube has been confirmed experimentally [85]. The size effect of a small drop on Laplace pressure has been elucidated theoretically [41, 43]. To date, understanding and in particular controlling water drop penetration are yet to be achieved [86, 87]. Several factors have not been investigated, such as the porosity, wetting angle of a drop, subjective angle of a meniscus (meniscus angle), drop volume, and pore size, among others. In the present research, we conduct an experimental study combined with theoretical analysis in order to identify and predict when a water drop penetrates into a hydrophobic surface with pored structures.

In order to study the behavior of penetration, we first discuss the morphology of a water drop - surface interface, illustrated in Figure 4.1. Here in Figure 4.1a, a drop has two air-water interfaces: one is a curved drop surface having the wetting angle (θ_d) on the pored surface, and the other is a meniscus in a pore. The meniscus forms the subjective angle (θ_m) between the pore wall and the air-water interface, which is defined as a meniscus angle. The curved drop surface may generate water penetration into a pore due to Laplace pressure [32, 88]. A meniscus produces capillary pressure, which depends on pore size and meniscus angle (θ_m) formed in the wall of a pore. When the meniscus angle is less than 90°, the pressure of a liquid is lower than the external atmosphere pressure, and its pressure difference always drives a water drop into a pore. When the meniscus angle is over 90°, i.e., hydrophobic, the pressure by a meniscus is

larger, and it may prevent water penetration. Liquid penetration depends on drop radius (R_d) or volume (V_d), pore size (d) and two angles (θ_d, θ_m) of a drop and a meniscus. Based on previous research, to determine the penetration of a water drop into a hydrophobic pore, the force balance condition (or net force F_{net}^S) of a drop on a single pore in the initial state was considered [43, 89]. This equation is expressed by

$$F_{net}^S = \frac{\pi\gamma d^2}{2R_d} + \rho g R_d(1-\cos\theta_d)\frac{\pi d^2}{4} + \pi d\gamma\cos\theta_m > 0 \qquad (4.1)$$

Here, γ is surface tension of water (72.86 mNm^{-1} at 20 ºC [90]), ρ is density of water, g is gravitational acceleration, and $R_d(1-cos\theta_d)$ is the height of a water drop. This equation contains three forces (from left to right): Force (F_D) from the curved surface of a small drop due to Laplace pressure, gravitational force (F_G) of a drop, and force (F_M, same as surface tension) by a meniscus in a pore. Gravitational force (F_G) of a drop into a pore is expressed by hydrostatic pressure by gravity, which can be neglected when the size of a drop is smaller than capillary length [83], because gravitational force was much smaller than the other two forces in the initial state. When a surface is hydrophobic (θ_d, θ_m > 90º), force (F_M) by a meniscus has upward direction, and it will interrupt water penetration. However, when a drop is small enough to make larger Laplace pressure than capillary pressure by a meniscus, its penetration can occur due to the positive net force having downward direction.

In this research, we investigated spontaneous penetration of a water drop into a hydrophobic single pore and/or vertically aligned multiple pores. Two parameters were studied, the drop volume and the pore size. Experimental results were analyzed using

force balance equation. The wetting behavior, penetration of a water drop, and net force were analyzed. Details are provided in the following.

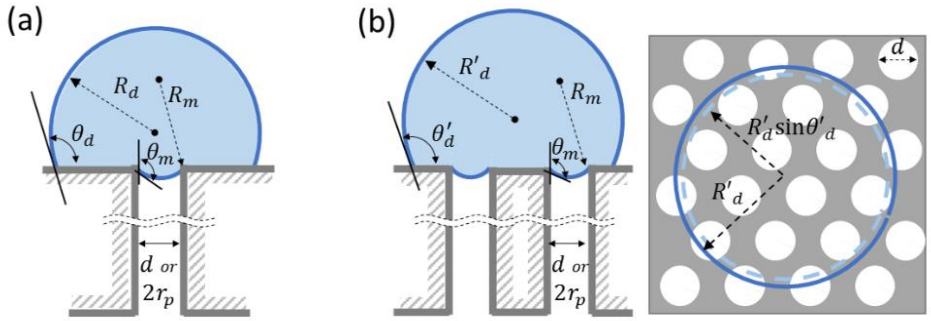

Figure 4.1 Schematics of a water drop on hydrophobic pored surface: (a) a single pore and (b) multiple pores

4.2. Experimental

In order to evaluate the behavior of a water drop on a pored surface, the drop volume and the pore size were controlled. For penetration experiments, single-pored and multiple-pored samples were prepared that have cylindrical and straight-edged pores. In multiple-pored samples, pores were randomly aligned with different pore densities. Samples were prepared by polymer casting [91], and pores were made by using wires with different diameters from 54 μm to 800 μm. After casting, wires were removed by swelling using ethanol/hexane mixture. To make a hydrophobic pore which wetting angle is over 90º, Polydimethylsiloxane (PDMS, Sylgard-184, Dow Corning Co.) was used. PDMS is a widely used, transparent, hydrophobic polymer [92, 93], so that water penetration and meniscus in a pore can be easily investigated. Pore lengths of single-

pore samples and multiple-pore samples were approximately 10 mm and 4 mm. Both sides of pores are exposed to the air.

The wetting angle and water penetration were measured 5 times at each water drop using a home-made goniometer which consisted of 30 fps camera, micro-syringes, and an xyz-control table. The volume of a water drop was ranged from 0.5 μL to 15 μL. The wetting angle of a water drop was usually decreased with time. Wetting angle measurement and penetration experiment were recorded for 1 minute.

4.3. Results and discussions

4.3.1. A water drop on a single pore

Following the steps discussed earlier, a water drop on a single pore was examined. When a drop was put on the pored surface, it formed two curvatures of air-water interface: the curved surface outside the pore and the meniscus inside the pore. The wetting angle against pore size is shown in Table 4.1. Here wetting angles are similar or a little larger than the wetting angle (109.6 ± 2.2^{o}) on PDMS flat surface. The larger the pore size, the bigger the wetting angle.

The behavior of the water drop on a single pore was studied, and results are shown in Figure 4.2. Figure 4.2a shows a relatively larger drop on a single pore that stays on the surface, i.e., in stable state. Figure 4.2b shows a smaller drop penetrated into the pore forming a meniscus. The stable and penetrated drop was further studied against the pore size and the drop volume. Results are shown in Figure 4.2c. On the right side, the drop stayed on the surface, while on the left, it penetrated. The boundary including black lines

has mixed state having stable drops or penetrated drops. Interestingly, it is seen that there is a parabolic relationship between the pore size and the drop volume. This plot represents a critical condition.

Why there is a critical condition? As discussed earlier, there are several forces acting on a water drop. The net force is followed by Eq. (4.1). The net force is believed to be the driving force for the stability of a water drop. When the net force is positive (>0), the drop penetrates. For simplicity, we make two assumptions. First, the wetting angle of (θ_d) of a drop on a single pore is the same as the wetting angle (θ_Y) on a PDMS flat surface which follows Young's equation. Second, the meniscus angle (θ_m) is assumed the same as θ_Y. Though the meniscus angle is not clearly defined [41, 89], it can be considered to be θ_Y in a quasi-static case. Based on these assumptions, Eq. (4.2) is emerged as a simplified force balance equation of a drop on a single pore:

$$\frac{d}{2}\left[\frac{1}{R_d}+\frac{\rho g R_d(1-\cos\theta_Y)}{2\gamma}\right] > \cos(\pi-\theta_Y) \tag{4.2}$$

The equilibrium state of this Eq. (4.2) shows the critical condition for penetration, which depends on three important factors: radius or volume of drop (R_d or V_d), pore size (d) and wetting angle (θ_f). This critical condition between the pore size and the drop volume follows almost a parabolic relationship, which was calculated by $R_d = [3V_d/\pi(2 - 3\cos\theta_Y + \cos^3\theta_Y)]^{1/3}$ in Eq. (4.2). The critical volume of a water drop is the maximum volume for penetration into a specific pore. The critical diameter of a pore is the minimum diameter that a specific water drop can enter into a pore. Figure 4.3 shows all forces (F_D, F_G, F_M, F_{Net}) of different volumes of water drops (1, 5, 10 µL) when the

wetting/meniscus angle are 110°. Net force is dominated by Laplace pressure of the curved surface of a drop and the surface tension of a meniscus. When the net force of each drop is zero, each critical diameter is calculated. Critical diameter of a pore increases as the increase of drop volume.

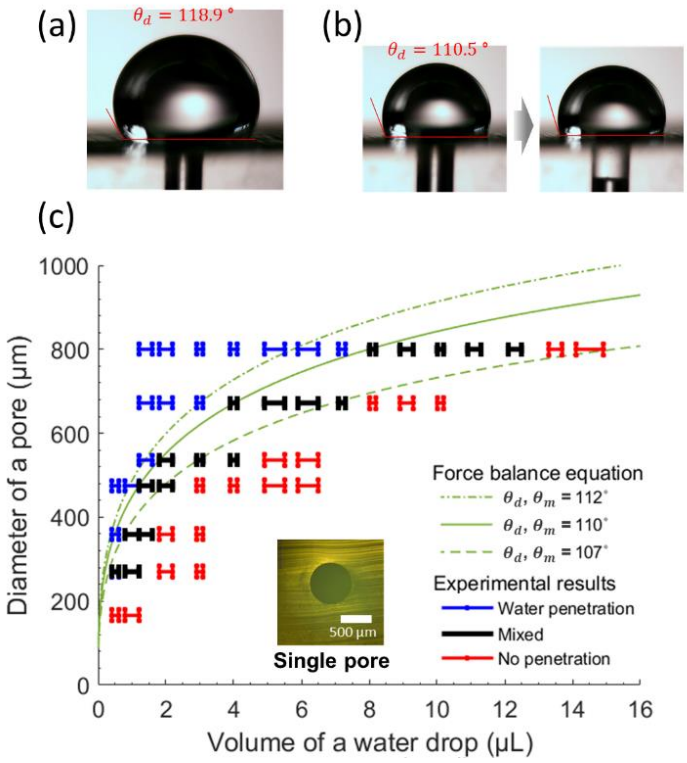

Figure 4.2 Penetration result on single-pored samples; (a) 7 μL drop, (b) 3 μL drop on a single pore (d = 672 μm) and (c) penetration result and theoretical result at different wetting/meniscus angles

4.3.2. A water drop on multiple pores

A water drop on multiple pores was examined. Experimental results in Figure 4.4 shows a similar trend as that shown in single-pored samples. In Figure 4.4c, the boundary separates stable and penetrated water drops in the same fashion (Figure 4.2c). As marked with black lines, they lie on right side more than that of single-pore samples. It means that the critical condition on multiple-pored samples has larger drop volume than that of single-pore samples.

Next, we discuss about the driving force for penetration on multiple pores. In such case, a drop covers several pores on a surface like Figure 4.1b. If it can enter any of them, it is considered as penetration. Theoretical approach toward penetration of a water drop on multiple pores can be regarded as the same as the penetration into a single pore. Net force (F_{net}^{M}) of a drop on multiple pores is expressed by

$$F_{net}^{M} = N\left[\frac{\pi\gamma d^2}{2R'_d} + \rho g R'_d(1-\cos\theta'_d)\frac{\pi d^2}{4} - \pi d\gamma\cos(\pi-\theta_m)\right] > 0 \qquad (4.3)$$

Here N is the number of pore in contact area between a water drop and a porous surface, which is calculated by contact area ($n\pi R_d'^2 \sin^2\theta'_d$) and pore density ($n$). A net force is the result of all forces acting on the surface area within a pore. In Eq. (4.3), all parameters remain the same such that the net force on multiple-pores can be multiplied by the number, N. Though the wetting angle (θ'_d) and radius (R'_d) of a drop on multiple pores are different from those on a single pore (Table 4.1), its net force is then calculated as N times of that on a single-pore sample.

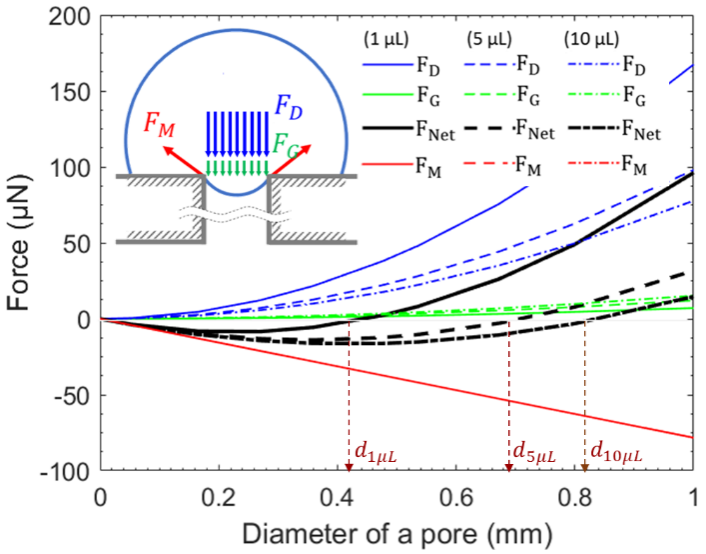

Figure 4.3 Forces of a water drop vs. diameter of a pore at different volumes of drops for penetration. The values of $d_{1\mu L}$, $d_{5\mu L}$, and $d_{10\mu L}$, are the critical diameters for penetration in each drop volume.

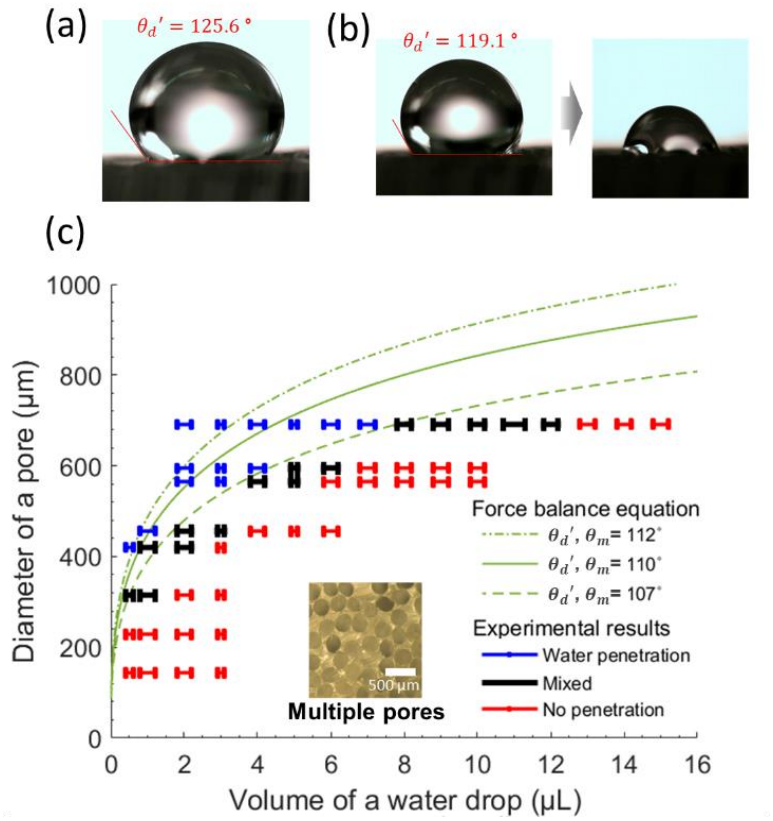

Figure 4.4 Penetration result on multiple-pored samples; (a) 13 μL drop, (b) 6 μL drop on a single (d = 691 μm, n = 1.8 pores/mm^2), and (c) penetration result and theoretical result at different wetting/meniscus angles

4.3.3. Shift of the critical condition

The critical conditions are affected by several factors. The boundaries (black lines in Figure 4.2c and 4.4c with stable drops or penetrated drops on single-/multiple-pored surfaces have a wide range. It can be explained by the variation of PDMS wetting angle (109.6 ± 2.2º), except those of smaller pore samples under 400 μm. But the boundaries on a single pore and multiple pores are located in the right side in Figure 4.5, i.e., small

pore size and large drop volume, based on the critical condition calculated at the average wetting/meniscus angle of 110º. It can also be explained by the reduction in wetting angle. When a drop is put on a surface, based on experimental results, the wetting angle decreases in time. When both angles (θ_d and θ_m) of a drop and a meniscus decrease in time, the critical condition is shifted to the right. This phenomena is due to the reduction of surface tension of a meniscus, and the decrease of meniscus angle (θ_m) that is more dominant to the net force.

According to Eqs. (4.1) and (4.3), the wetting angle of a drop has effects on the critical condition. Table 4.1 shows the increase of wetting angles in experiments and calculation. Surface porosity affects wettability, which depends on surface energy and the contact area ratio of air-liquid and air-solid. Based on Cassie-Baxter's model [35], a wetting angle on a porous surface is defined as Eq. (4.4). The f_{S-L} is the total area of solid-liquid interface, and f_{A-L} is the total area of air-liquid interface in a plane geometrical area of the rough surface.

$$\cos\theta_{CB} = f_{S-L}\cos\theta_Y + f_{A-L} \tag{4.4}$$

As shown in Figure 4.5, the critical conditions on a single pore and multiple pores were predicted by the force balance equations considering average wetting angles calculated by Cassie-Baxter's model. Surface porosity by multiple pores increases wetting angle and net force for penetration by decreasing the drop radius, and then it shifts the critical condition toward right in Figure 4.5b.

Compared with two groups of wetting angles measured in case of a stable state (i.e. no penetration) and penetration (Table 4.1), wetting angles of stable drops are slightly

larger than those with penetration, even though they have different drop volumes. This is also due to the driving net force. When the water drop is stable, the net force is negative (<0), so it makes a drop stay on a pore. When the net force becomes positive (>0), it pulls down the drop and results in reducing the wetting angle and subsequent penetration. There might be other factors affecting the critical conditions discussed above, such as irregularity of pores, imperfection of surface morphology, and center alignment of pores/drops. This research provides solid proof of stability and penetration of a water drop on single and multiple pores of various sizes. The critical condition for stability and/or penetration is an important factor for surface optimization.

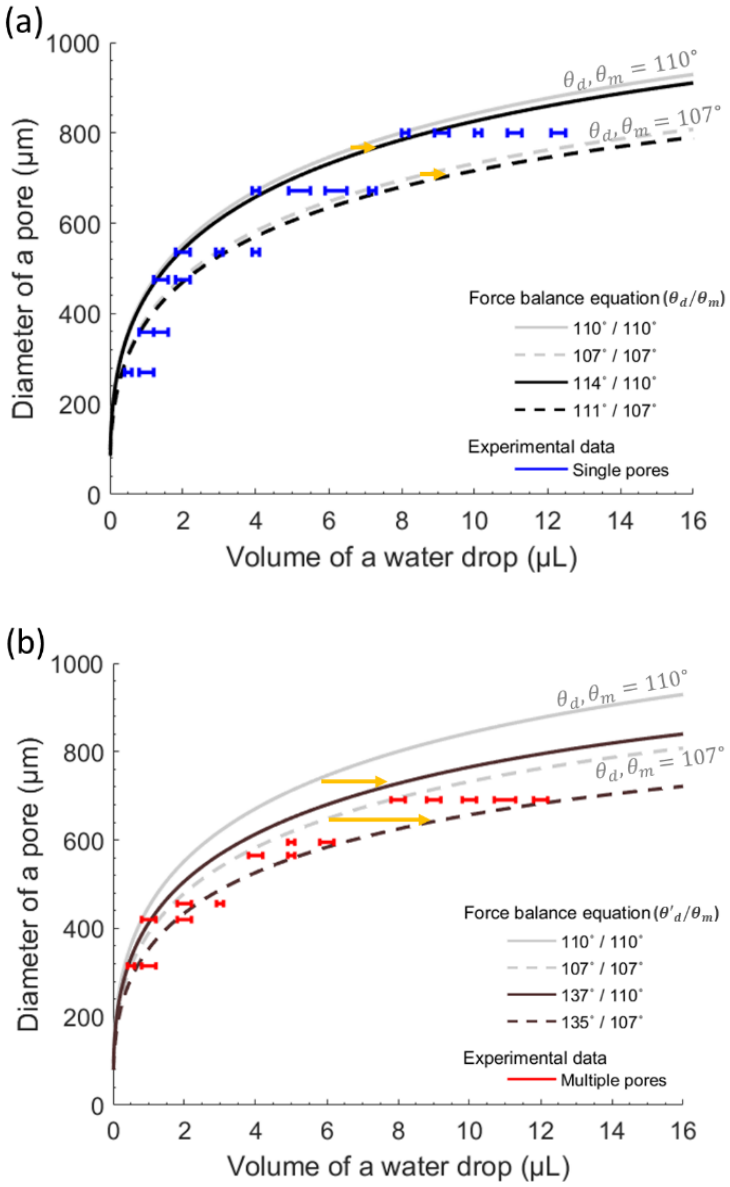

Figure 4.5 Shift of the critical condition by wetting/meniscus angles based on Table 4.1; (a) on a single-pore and (b) multiple-pores

Table 4.1 Initial wetting angles of a drop on pore samples, measured by penetration experiment and calculated by Cassie-Baxter's model

Single-pored samples			Multiple-pored samples			
Pore size (μm)	WA [1] (°)	WA by CB [2] (°)	Pore size (μm)	Density (Pores/mm^2)	WA [1] (°)	WA by CB [3] (°)
800	108.1 / 116.6	113.3 ±3.3	691 ±22	1.81 ±0.1	118.6 / 125.4	141.9 ±1.1
672	110.3 / 114.3	113.8 ±3.3	595 ±19	2.25 ±0.1	116.4 / 123.1	138.7 ±1.2
536	109.0 / 113.2	114.2 ±3.3	571 ±16	2.57 ±0.5	120.1 / 124.0	140.6 ±1.1
475	111.4 / 113.5	114.4 ±3.3	456 ±10	3.05 ±0.3	113.8 / 124.5	131.8 ±1.4
359	108.1 / 113.0	114.6 ±3.3	420 ±10	4.49 ±0.3	116.8 / 125.7	138.5 ±1.2
270	109.6 / 111.7	114.7 ±3.3	315 ± 8	6.99 ±0.7	122.3 / 126.5	134.2 ±1.3
166	- / 111.2	114.8 ±3.3	229 ± 7	13.85 ±0.5	- / 122.8	135.6 ±1.3
54	- / 110.4	114.9 ±3.3	144 ± 8	31.54 ±2.8	- / 128.3	132.6 ±1.4

For calculation, wetting angle (WA) on PDMS flat surface is 109.6 ±2.2°.

[1] WAs of water drops in case of penetration / no penetration, measured by penetration experiments.

[2] WA calculated by Cassie-Baxter's model **[35]** using critical volume on each pore.

[3] WA calculated by Cassie-Baxter's model considering pore size and pore density.

4.4. Conclusions

In the present research, we investigated the stability and penetration of a water drop into a hydrophobic polymer with various sized pores. Experiments were conducted by using different volumes of water drops ranged from 0.5 to 15 μL, on different pore sizes (< 800 μm diameter). Results showed a clear trend with the critical condition that

distinguishes a water drop being stable and being penetrative. With small pores and large drop volumes, water drops stay on pored surfaces. With large pores and small drop volumes, they penetrate into the surface. Theoretical analysis was conducted based on the force balance equation and Cassie-Baxter's model. Results showed that the transition for a water drop from stable to penetration is driven by the net force. This net force is affected by the pore size and droplet volume. The theory plots match well with experimental ones. When we design porous materials dealing with liquid penetration such as filters, nozzles, and textures, the relation between penetration and wettability is important. In those cases the surface-pore size and the amount of water are factors to be considered in order to optimize the geometry of porous materials.

CHAPTER V

A KINETIC STUDY OF SPONTANEOUS PENETRATION OF WATER INTO A HYDROPHOBIC PORE

The spontaneous penetration of a water drop going into hydrophobic single-pored samples of varying inside and outside diameters was studied. During penetration, the radius of a water drop, its contact angle, the contact radius, and the penetration length inside a pore were measured against time. Experimental results showed that a water drop on a smaller pored sample has longer penetration time than on a bigger one due to viscous drag. A pored sample with a small outside radius (thin tube) leads to a fast penetration rate presenting a parabolic trend in penetration in time. The maximum penetration rate was found to be a characteristic value when the contact angle is 90°. This is mainly due to the minimum radius of the drop attributing to Laplace pressure as the driving force. Two factors were identified affecting penetration. The first is the receding contact angle leading to stick-slip-like motion of a water drop. The second is the outside radius of a pored sample, which affects the penetration rate and trend. These relations were in correlation with the theoretical analysis through geometrical consideration of the capillary system, volume conservation and momentum conservation. The initial contact angle and radius of a drop were determined by the outside radius of a pored sample, which changed Laplace pressure against time in order to influence the penetration trend and rate. This indicated that a thin tube promoted fast penetration, and the point of the maximum penetration rate was shown later during the penetration.

Understanding the effects of outside radius and receding contact angle in the kinetic aspect of the drop penetration into a hydrophobic pore is fundamentally important. This research is beneficial to design porous materials and to control the wetting and penetration process.

5.1. Introduction

Penetration of a liquid drop into porous media is a common and fundamental process in nature and daily life. Examples are the capillary action of plants, oil penetration into rock, and a cloth and soil being wet by the rain. Industrial applications such as ink-jet printing [79], paper/textile manufacturing [76, 94], wicking [95], micro/nano-fluidics [42, 81] and oil recovery [80], involve the penetration of a small drop into capillary systems [41]. The study of the dynamics of capillary penetration was firstly reported by Lucas [28] and Wash-burn [29]. They studied a quasi-steady-state laminar flow of a Newtonian liquid considering an infinite reservoir, neglecting the inertia effect and fluid resistance [41]. On the basis of this model, many researchers have developed capillary phenomena. The penetration of a finite drop into a capillary tube was reported by Marmur [41, 43]. When a finite drop contacts a pored surface, it forms two curvatures between air-water interface: the surface outside the pore and the meniscus inside. Capillary penetration is driven by the pressure difference between a small drop and the meniscus in a pore. A smaller and/or more spherical drop increases the pressure difference by increasing the Laplace pressure of a drop. Consequently, as the pressure difference is increased, the process of penetration is enhanced.

In liquid penetration, both the drop radius (or volume) and pore size determine the capillary penetration and its kinetic behavior. To date, understanding and controlling the capillary penetration of a small drop into a hydrophobic pore need to be further achieved [85, 89]. While a small pore increases the viscous resistance, a large pore and a small drop involve the relatively rapid penetration of a liquid drop in the initial stage [43]. Kinetics of penetration related to morphological factors and wetting characteristics have not been reported. Marmur and Densuk defined two limiting cases of the moving contact between a drop and a surface and contact angle hysteresis [41, 96]. The first case is the constant contact area (i.e. pinning of the contact circle), and the contact angle decreases as the penetration processes. The second case is that the contact angle on a surface remains constant throughout the penetration process and the contact circle recedes toward the center of the drop (i.e. depinning of contact circle). Though this research was conducted about the contact line and contact angle hysteresis [84, 96-98], the kinetic aspect of the moving contact circle and contact angle hysteresis related to the penetration rate were not well explained. The penetration of a water drop into a pore is similar to the process of receding contact angle (RCA) measurement by volume changing method [99, 100]. When the volume of a drop decreases, the contact angle just before the contact circle is receding is defined as receding contact angle. Sometimes, this stick-slip motion is shown during drop evaporation [101-104]. Penetration rate closely relates to the drop radius changed by receding contact angle and the motion of contact circle. For example, in the transport of water or oil into porous media (soil, rock, fabrics, filters, or micro fluidic devices), the initial contact area between a drop and a porous

surface may affect the drop's shape, and the associated driving pressure changes the penetration. In addition, the structure and thickness of a porous media are related to penetration.

In the present research, an experimental study of the penetration of a water drop was conducted on a hydrophobic pore of varying inside and outside radii (i.e. tube-shaped sample). The purpose of changing the outside radius was to verify the effect of initial contact area between water and a solid. Experiments revealed that the penetration rate increases with the decrease of the outside radius. The penetration length with the maximum penetration rate, i.e., the maximum penetration point, was identified. To understand principles behind this, kinetic analysis was carried out based on geometrical consideration of a capillary system, volume conservation and momentum conservation based on Lucas-Washburn theory. It was found that the initial contact circle between a drop and a surface and the moving boundary determine the penetration rate. It means that the outside radius of a pore and receding contact angle are parameters affecting the penetration trend and rate. This research is beneficial to design porous materials with desired penetration.

5.2. Experimental

Samples were prepared using a hydrophobic polymer, Polydimethylsiloxane (PDMS, Sylgard-184, Dow Corning), which is widely used for the fabrication of micro-fluidic devices [92, 93]. Each sample had a cylindrical and straight-edged pore, and both sides were exposed to the air. The pore radius ranged from 294 to 444 μm. As the first step, a

single pore was selected as a simplified system to observe the penetration process. The volume of water drops was controlled from 1 to 5 μL, which was smaller than the critical volume for spontaneous penetration [83, 105]. Pores were fabricated by using metal wires and hollow cylinder tubes. After polymer casting, wire and tube were removed using ethanol/hexane. PDMS, a transparent hydrophobic polymer, was used so that penetrated water and its meniscus in a pore were clearly observed.

A water drop was put on a single-pored sample and penetrated into the pore. The penetration process was recorded using by the home-made goniometer which consists of 30 fps camera, micro-syringes and xyz-control table. The starting time was set when water began to penetrate into a pore, and the end time was set when the penetration length became almost constant. In every step, the contact angle of a drop, drop radius and penetration length were measured by using ImageJ software. To understand this capillary penetration system, its description is provided here. As shown in Figure 5.1, this system has several characteristic dimensions and variables. The drop in the form of a spherical segment having an instantaneous radius, R_d, and contact angle (CA), θ_d, has contact on a pored sample of an inside radius, r_p, and an outside radius, r_t. Its contact formed a circle between the drop and the surface. The radius of the contact circle is R_c (i.e. contact radius). Initial radii (R'_{d0} and R'_{c0}) and its contact angle (θ'_{d0}) vary depending on the outside radius of a sample as shown in Figure 5.1b. The penetration is determined by measuring penetration length, l.

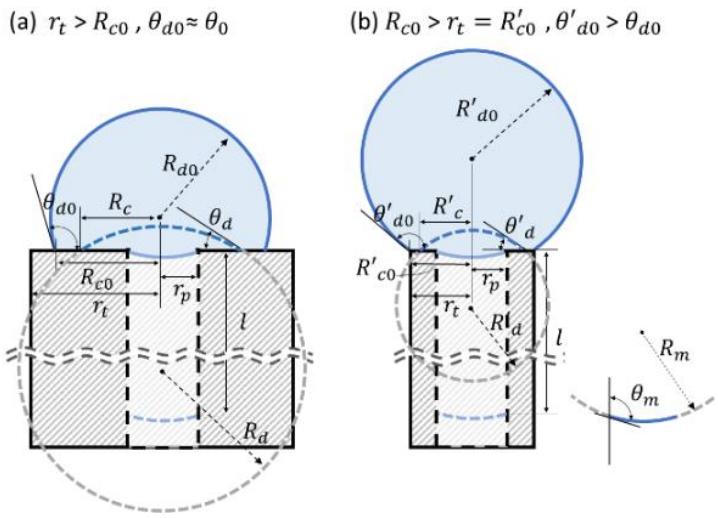

Figure 5.1 Capillary penetration system of a drop on a pored surface: (a) when $r_t > R_{c0}$, and (b) when $r_t < R_{c0}$.

5.3. Results and discussions

5.3.1. The process of penetration

When a water drop was put on a pored PDMS sample, it penetrated into the pore and stayed stable, as shown in Figure 5.2. Figure 5.2a shows the penetration on the thick tube-shaped pored sample when the outside radius is larger than the initial contact radius ($r_t > R_{c0}$). Figs. 5.2b/c show the penetration on thin tube samples with various outside radii when $r_t < R_{c0}$. The effects of an outside radius was evaluated on the penetration. The drop on a thin tube sample (i.e. a small outside radius) has a more spherical shape. There was a fast penetration observed. (Figure 5.2c). Geometrically, the outside radius (r_t) of a sample determines the initial contact area between a drop and a pored surface. The effect of a drop radius on contact angle is discussed later.

Here we discuss the effects of the drop radius and contact angle on pored samples of various outside radii. (See results in Figure 5.3a). The outside radius changed the initial contact angle and drop radius, and it affected the penetration time. As mentioned earlier, since the drop radius is closely related to Laplace pressure, the change of its radius is an important factor to estimate the penetration process. In Figs. 3b-d, dimensionless values are used such as $\Theta = \theta_d/90$, $\mathcal{R}_d = R_d/R_{d0}$, $\mathcal{L} = l/l_{max}$, $\mathcal{R}_c = R_c/R_{c0}$ and $\mathcal{T} = t/t_{total}$, to compare the experimental results. The change of the drop radius displays a complex behavior. Each outline picture in graphs shows the drawing lines of the drop and the penetrated water in a pore, which explains the penetration process at time intervals.

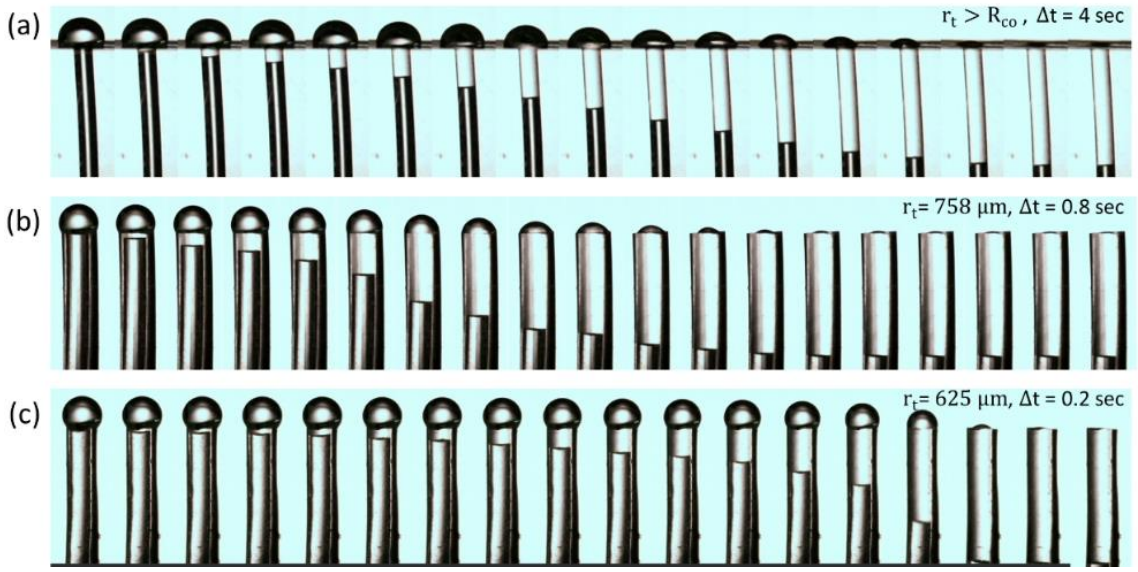

Figure 5.2 Capillary penetration of a water drop into PDMS single-pored samples of various outside radii (r_t). Pore size (r_p) is 394 µm and the drop volume (V_0) is 2.5 ± 0.2 µL.

During penetration, the volume of the drop on a pore continuously decreases, and the penetrated water in a pore increases. Based on volume conservation ignoring water evaporation, the volume of a drop and the volume of penetrated water into a pore are correlated with each other like Eq. (5.1).

$$V_0 = V_m + \frac{\pi}{3} {R_d}^3 \left(2 - 3\cos\theta_d + \cos^3\theta_d\right) + \pi {r_p}^2 l \tag{5.1}$$

Here, V_0 is the initial volume of a water drop, which is basically constant. V_m is the volume made by the concave curvature of the meniscus in a pore, which is comparatively too small to be neglected. The contact angle (θ_d) of a drop, drop radius (R_d) and penetration length (l) are time-dependent valuables. During penetration, there seem to be more than one parameters dominating, such as stick-slip motion (i.e. pinning and depinning) of the contact circle and receding contact angle (RCA). These will be discussed next.

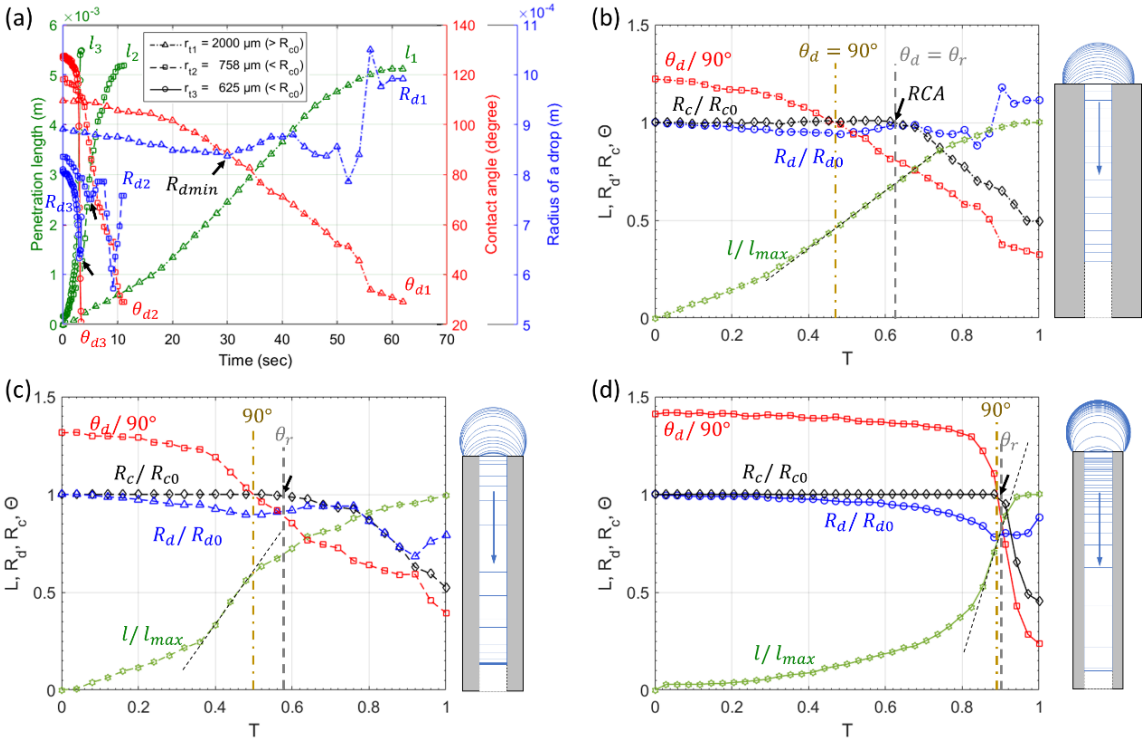

Figure 5.3 Plots of penetration over time (r_p = 394 μm, V_0 = 2.5 ± 0.2 μL): (a) time versus contact angle, penetration length, drop radius and contact radius; (b) dimensionless time (T) versus dimensionless values (L, R_d, Θ, R_c) when rt = 2000 μm (r_t > R_{c0}); (c) when r_t = 758 μm (r_t < R_{c0}); (d) when r_t = 625 μm (r_t > R_{c0}). The arrows in Figure 5.3a point to the local minimum radius of each drop. The arrows in Figure 5.3b/c/d mark the beginning of decreasing contact line/contact radius (R_c).

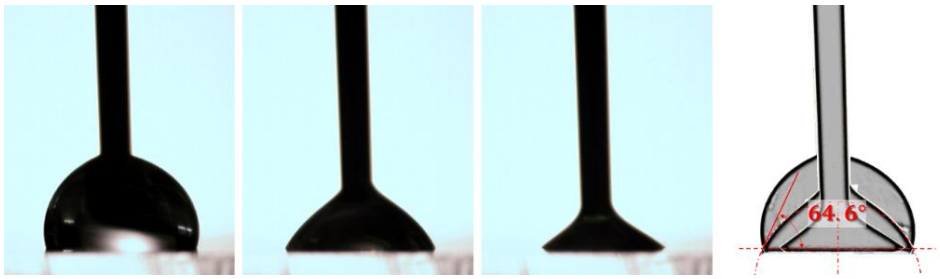

Figure 5.4 Receding contact angle on PDMS flat surface by volume changing method

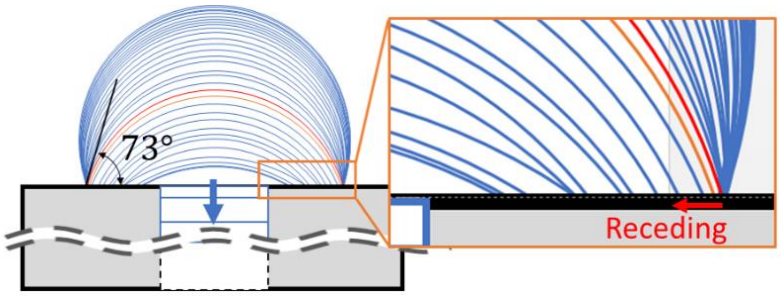

Figure 5.5 The drawing line of drop penetration and the receding contact angle (RCA) of PDMS pored sample

5.3.2. The receding contact angle (RCA)

During penetration, the contact circle was found to have stick-slip-like motion. It was found at the beginning of penetration, when the radius of contact circle (R_c) remains unchanged (i.e. pinned on the surface). The "pinned" drop remains on the surface while the contact angle decreases. This phenomenon is called contact angle hysteresis [104]. At a certain angle, the contact circle becomes depinned and starts to decrease (black arrows in Figure 5.3b/c/d). This angle is similar to the receding contact angle (RCA)

measured by the volume changing method. According to previous research [106, 107], the RCA of flat PDMS is 64°~ 81°, which is similar to the RCA (75 ±5°) here. In this study, the RCA on a pored sample is based on the spontaneous penetration of a water drop. The volume decreasing rate is not linear, and it is determined by the pore size and the drop volume. Furthermore, the water drop is drained through the bottom. This observation was different from those of common methods using a needle attaching the top of a drop.

The penetration process is further examined in two cases. In the first case, a pored sample has a larger outside radius than the contact radius ($r_t > R_{c0}$). Figure 5.4 illustrates the evolution of the water drop during penetration. Figure 5.4a(i) was at the beginning of the penetration when there is no contact between the water drop with the surface. Figure 5.4a(ii) shows the initial state, and the contact angle is almost the same as Young's contact angle (YCA, θ_0=109.6 ± 2.2°). Then the water continues to penetrate into a pore. When the contact angle (CA, θ_d) decreases toward 90°, the drop radius (R_d) also decreases in the pinned contact circle. On the other hand, when CA decreases from 90° to RCA (θ_r), the drop radius naturally increases. In this process, the minimum drop radius (R_{dmin}) is observed in Figure 5.4a(iv). Its minimum radius of a drop is the same as the initial contact radius (R_{c0}). Subsequently, when CA passes through RCA, the contact circle becomes unpinned and its contact radius begins to decrease (Figure 5. 4a(v)). Usually, the drop radius increases, but sometimes it decreases irregularly due to non-uniform movements of the contact line on a surface and meniscus in a pore and/or surface imperfections. In the second case ($r_t > R_{c0}$), a thin tube sample shows the

similar behavior (Figure 5.4b). When comparing two cases, a thin tube sample with a small outside radius has larger initial contact angle and smaller drop radius. In Figure 5.4b(iv), when CA (θ'_d) = 90°, the minimum drop radius (R'_{dmin}) is the same as the outside radius (r_t) and also the initial contact radius (R'_{c0}). In this process, since the drop radius directly relates to Laplace pressure as the driving force for penetration, this minimum radius contributes to the fast penetration rate. If its RCA is larger than 90° ($\theta_r > 90°$), the unpinning of contact circle may start early with a relatively smaller drop radius, and its penetration may be faster without contact angle hysteresis.

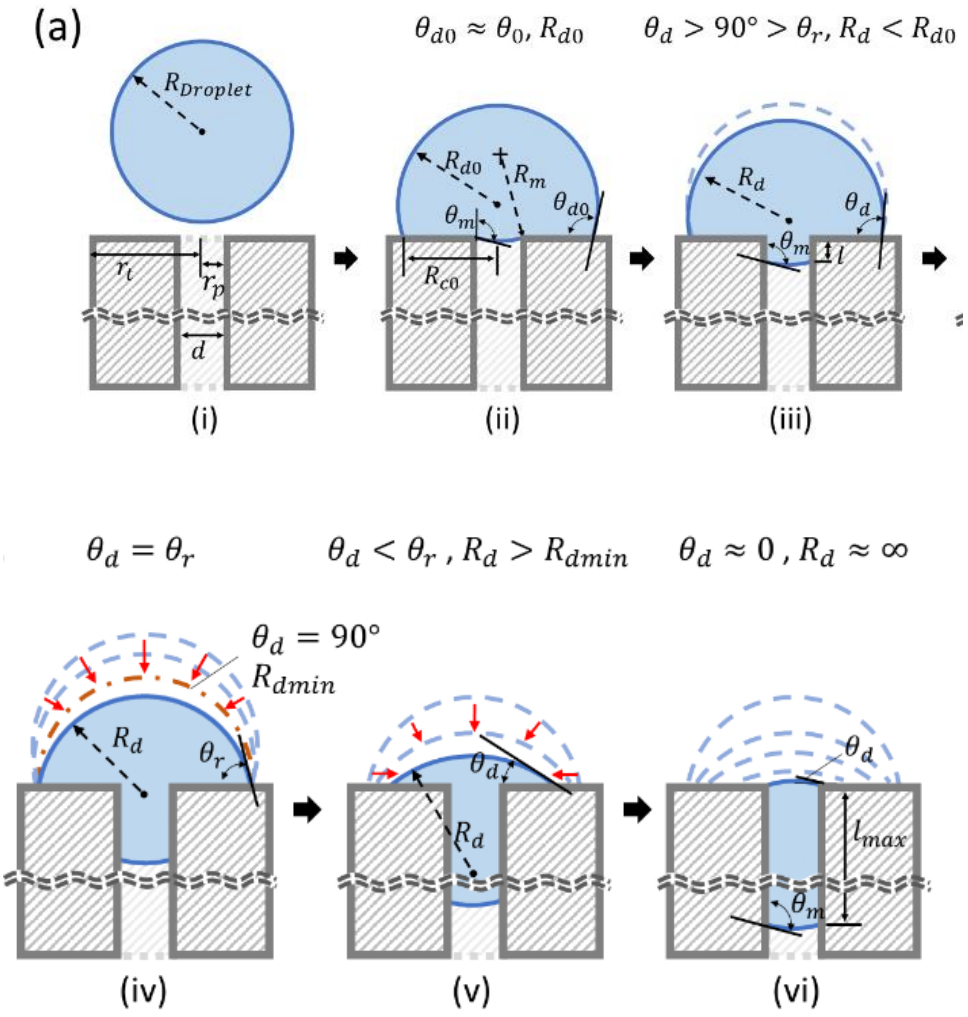

Figure 5.6 Schematics of the penetration process on a thick tube sample ($r_t > R_{c0}$)

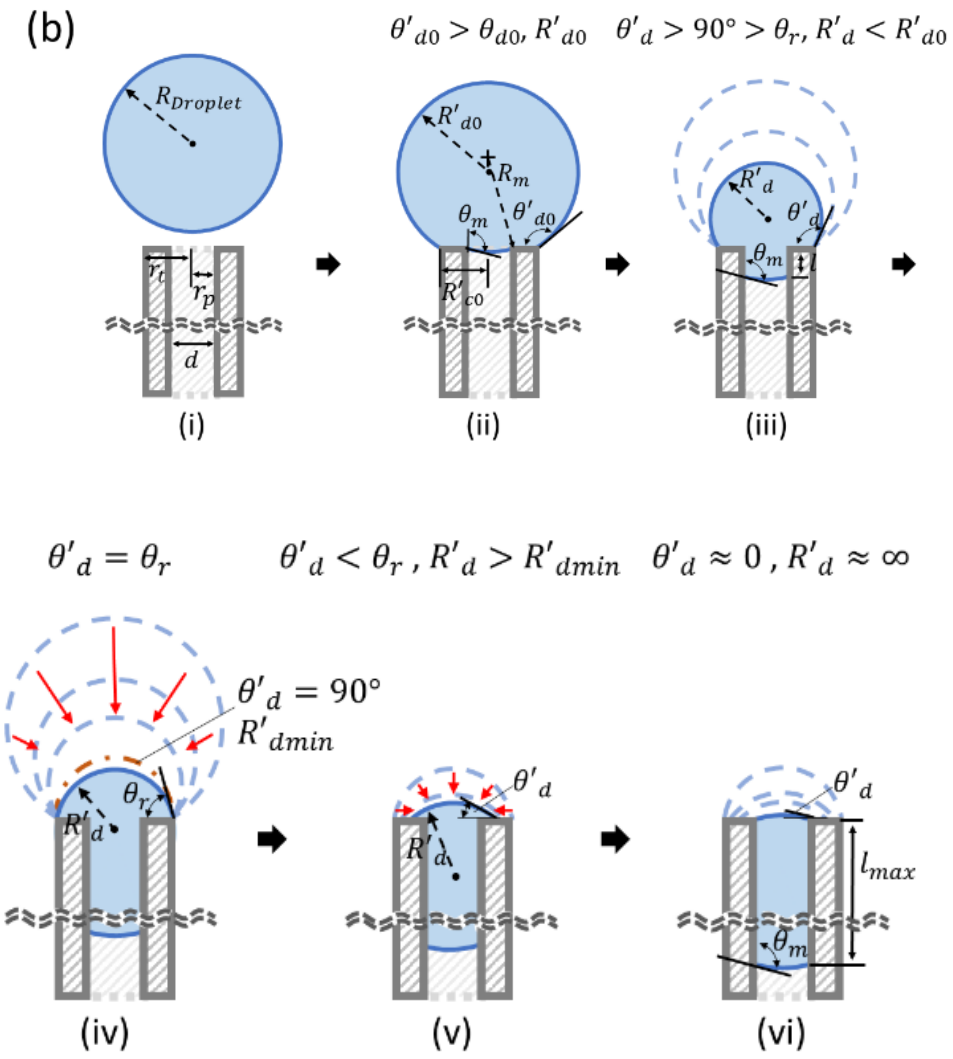

Figure 5.7 Schematics of the penetration process on a thin tube sample ($r_t < R_{c0}$).

The above behavior can be expressed through the following equations. Based on volume conservation principle, the Eq. (5.1) is differentiated by time, leading to Eq. (5.2). Here the penetration rate (dl/dt) is associated with the change in contact angle (θ_d) and a drop radius (R_d), which are time-dependent valuables. In Eq. (5.3), when $\theta_d > \theta_r$, the penetration rate is dominated by θ_d and $d\theta_d/dt$. Here the contact radius (R_{c0})

is constant as $R_d sin\theta_d$. When $\theta_d < \theta_r$, the penetration rate becomes a function of θ_d and contact radius ($R_c \neq constant$).

$$\frac{dV_0}{dt} = \frac{d}{dt}\left[\frac{\pi}{3} {R_d}^3 \left(2 - 3\cos\theta_d + \cos^3\theta_d\right)\right] + \pi {r_p}^2 \frac{dl}{dt} = 0 \tag{5.2}$$

$$\begin{aligned} &\text{At } \theta_d > \theta_r \text{ and } R_d = R_{c0}/\sin\theta_d, \ \frac{dl}{dt} = -\frac{{R_{c0}}^3}{4{r_p}^2}\sec^4\left(\frac{\theta}{2}\right)\frac{d\theta}{dt} \\ &\text{At } \theta_d < \theta_r \text{ and } R_d = R_c/\sin\theta_d, \ \frac{dl}{dt} = -\frac{d}{dt}\left[\frac{{R_c}^3}{3{r_p}^2}\left(\frac{2 - 3\cos\theta_d + \cos^3\theta_d}{\sin^3\theta_d}\right)\right] \end{aligned} \tag{5.3}$$

5.3.3. Identification of maximum penetration rate

Penetration rate was measured by the slope of penetration length and time. During penetration, the water drop reaches a maximum rate (dl/dt). Figure 5.8 show the maximum penetration rate on various pore sizes and drop volume. In Figure 5.3b-d, each slope of dotted lines shows the maximum penetration rate. It was interesting that this rate was always found when CA=90º, and the drop had the local minimum radius (R_{dmin}), as discussed in Figure 5.4. When CA decreases through 90°, the slope begins to decrease. This relation is clearly observed in $\mathcal{R}_d$, $\mathcal{R}_c$ and $\mathcal{L}$ when CA is between 90° and RCA (θ_r) in Figure 5.3b-d. The relation between the penetration rate and a drop radius is in agreement with reports about capillary and viscous effects based on momentum conservation like Eq. (5.4) [94, 108].

$$\rho \frac{d}{dt}\left(l \frac{dl}{dt} \right) + \frac{8\eta}{r_p{}^2} l \frac{dl}{dt} = \frac{2\gamma}{R_d} + pgR_d(1-\cos\theta) + \frac{2\gamma\cos\theta_m}{r_p} \tag{5.4}$$

Ignoring gravitation force and inertia force, this relation can be simplified as

$$\frac{dl}{dt} = \frac{r_p{}^2}{8\mu}\frac{\Delta P}{l}, \quad \Delta P = \frac{2\gamma}{R_d} + \frac{2\gamma\cos\theta_m}{r_p} \tag{5.5}$$

Here, pressure difference (ΔP) is the driving force for penetration, which consists of the capillary pressure of a meniscus and Laplace pressure of a drop. Because the capillary pressure of a meniscus is assumed to be constant, the driving force mainly depends on the drop radius. When CA=90°, there is the maximum penetration rate with the minimum drop radius. The difference in the initial radius (R_{d0} or R'_{d0}) and the minimum radius (R_{dmin} or R'_{dmin}) (Figure 5.4) is seen to play an important role. The higher the difference, the faster the drop penetrates, and vice versa. In addition, the penetration length (l_{MP}) having the maximum penetration rate can be calculated based on volume conservation of a drop by the following equation.

$$l_{MP} = \frac{1}{\pi r_p{}^2}\left(V_0 - \frac{2}{3}\pi R_{d\min}{}^3 \right), \quad R_{d\min} = r_t \text{ at } r_t \le R_{c0} \tag{5.6}$$

5.3.4. Effects of outside radius

The outside radius of a pored sample was found to affect the penetration rate and trend. A drop with short penetration time was found not only on a large pore but on a pore of a small outside radius. As shown in Figure 5.5, the relation between time and penetration length has a logarithmic curve with a large pore and $r_t > R_{c0}$ (Figure 5.5a).

When $r_t < R_{c0}$, it has a parabolic relation (Figure 5.5b). The point (l_{MP}) of the maximum penetration rate is determined by the volume change when CA changes to 90° (Figure 5.9). That is, this point on thin a tube sample is shown later in the penetration process in Figure 5.5b. This relation between penetration length and the outside radius at the maximum penetration rate can be estimated using dimensionless values such as l_{MP}/l_{Total} and r_t/R_{c0}, like Eq. (5.7),

$$\frac{l_{MP}}{l_{Total}} = \left[1 - \frac{2\sin^3\theta_{d0}}{(2 - 3\cos\theta_{d0} + \cos^3\theta_{d0})}\left(\frac{r_t}{R_{c0}}\right)^3\right] \quad \text{at } r_t \le R_{c0} \tag{5.7}$$

In the case that the outside radius is relatively smaller, the point (l_{MP}) is shown later in Figure 5.6 and 5.11. After passing by this point, the penetration is suddenly slowed down. As shown in Figure 5.10, experimental result shows the same behavior.

Other possible factors affecting penetration are adhesion and friction. If there is low adhesion on the water-surface interface, the contact circle can be easily unpinned and recede fast. In case of high adhesion, the contact circle tends to maintain stable. The receding movement of contact circle may be comparatively slow, and the penetration is slowed down with the increase of a drop radius. This behavior should be dependent on surface properties such as wetting, adhesion, slip length and surface roughness that will be discussed here.

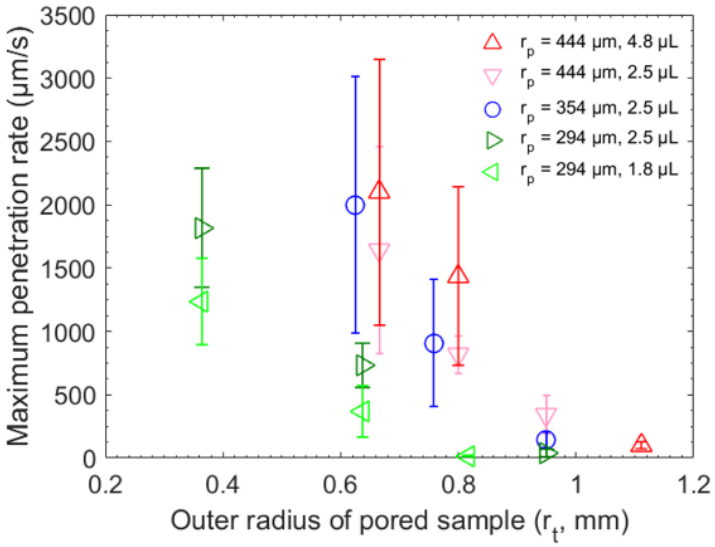

Figure 5.8 Maximum penetration rate versus outside radius in different sizes of pores

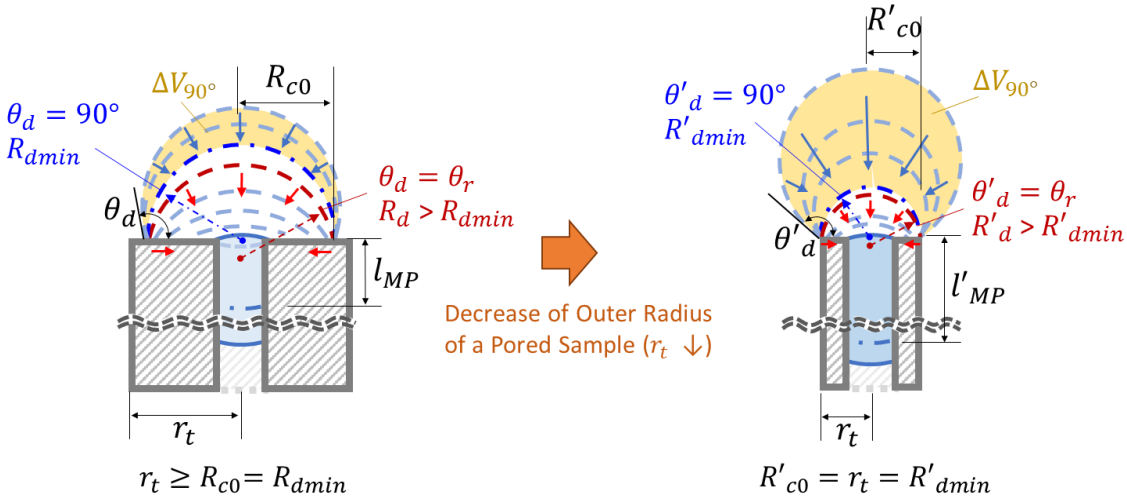

Figure 5.9 Schematics of the volume change of a drop on different outside radii when CA decrease to 90º

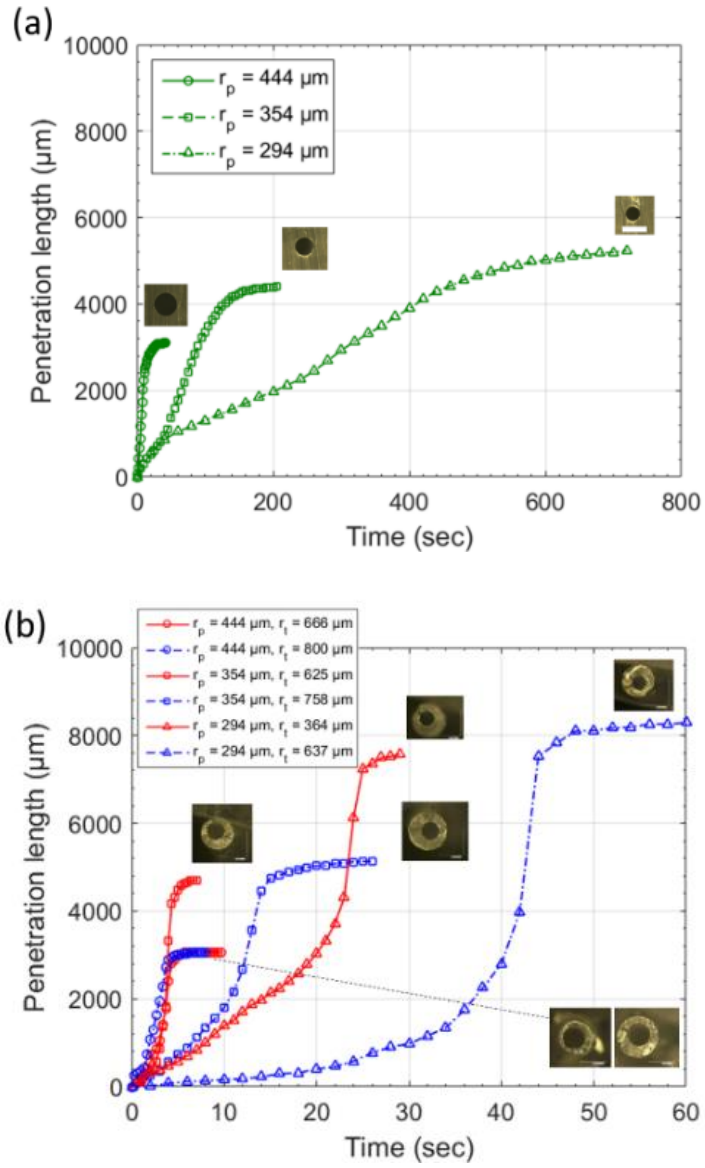

Figure 5.10 Plots of the penetration length over time: (a) $r_t > R_{c0}$ and (b) $r_t < R_{c0}$.

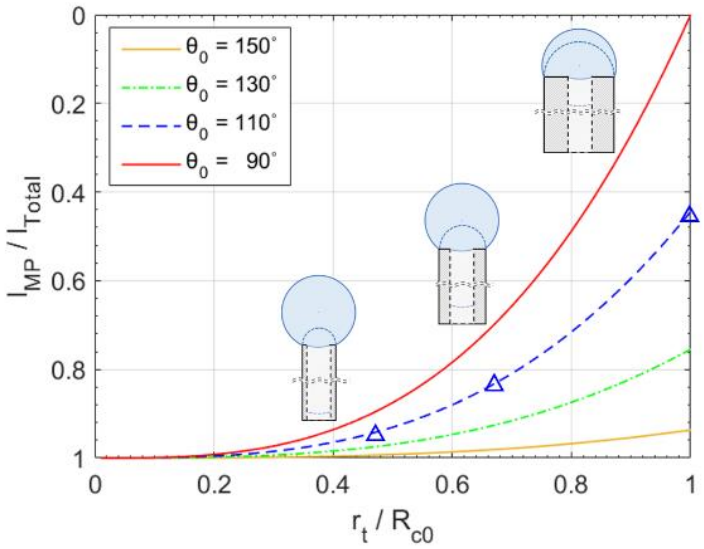

Figure 5.11 Plots of dimensionless penetration length (l_{mp} / l_{Total}) at maximum penetration rate and dimensionless outside radius (r_t / R_{c0}) at various Young's contact angle.

Finally, our results show that the radius of a drop, its contact angle, the outside radius and receding contact angle are important factors to control penetration. It is predicted that the surface morphology can affect penetration. Under the condition of a hydrophilic surface with a hydrophobic pore (Figure 5.7a/b), a rough surface increase wetting and promotes pinning. As such the penetration is lessened due to the decrease of Laplace pressure by the increase of a drop radius. Under the condition of a hydrophobic surface with a hydrophilic pore (Figure 5.7c-e), both the capillary pressure of a convex meniscus and the Laplace pressure of a small drop radius enhance penetration. This indicates that through surface modification, a controlled penetration can be achieved (Figure 5.12).

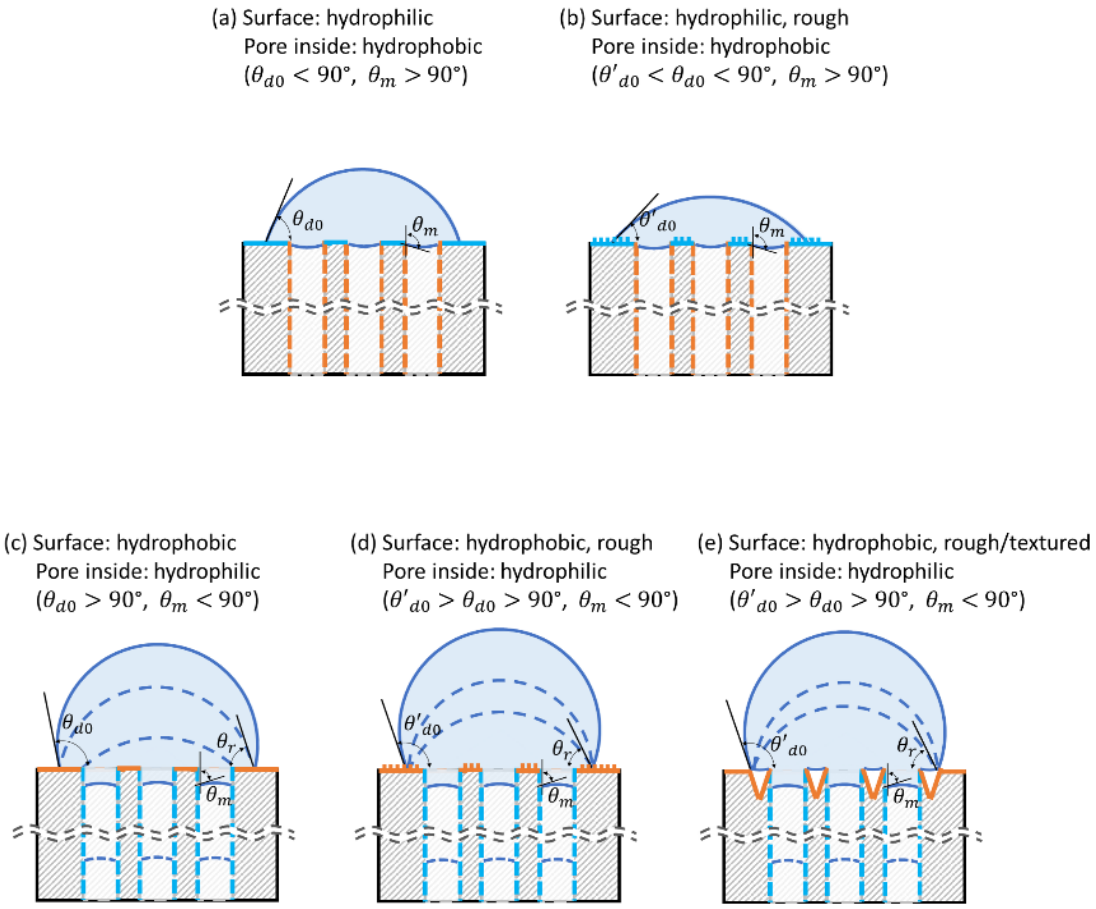

Figure 5.12 New design of capillary penetration system. Blue line is hydrophilic and brown line is hydrophobic.

5.4. Conclusions

In the present research, we investigated the spontaneous penetration of a water drop into hydrophobic single-pored samples of varying inside and outside radii. During penetration, the radius of a water drop, its contact angle, the contact radius, and the penetration length inside a pore were measured against time. Experimental results

showed that a water drop on a smaller pored sample has longer penetration time than on a bigger one due to viscous drag. A small pore (about 294 μm) with a small outside radius (364 μm) leads to a fast penetration rate (1818 ±470 μm/sec) presenting a parabolic trend in penetration in time. The maximum penetration rate was found to be a characteristic value when the contact angle is 90°. This is mainly due to the minimum radius of the drop correlating to Laplace pressure as the driving force.

Two factors were identified affecting penetration. The first is the receding contact angle leading to a stick-slip-like motion of contact circle. The second is the outside radius of a pored sample, which affects the penetration rate and trend. These relations were in correlation with theoretical analysis. Theoretical results revealed that the pinning contact circle made the minimum radius of a drop at CA=90º leading to the maximum penetration rate. It was proved by simplified momentum balance equation. Based on geometrical consideration, the initial contact angle and radius of a drop were determined by the outside radius of a pored sample, which changed Laplace pressure against time in order to influence the penetration trend and rate. It indicated that a thin tube sample of a small outside radius promoted fast penetration, and the point of the maximum penetration rate was shown later during the penetration. Understanding the effects of outside radius and receding contact angle in the kinetic aspect of the drop penetration into a hydrophobic pore is fundamentally important. This research is beneficial to design porous materials and to control the wetting and penetration process.

CHAPTER VI

CONCLUSIONS AND FUTURE RECOMMENDATIONS

6.1. Conclusions

This research investigated water-material interfaces of textured surfaces. Three areas of investigation was carried out: wettability and adhesion of super-hydrophobic surfaces of textured structures; stability of a water drop on single-pored and multiple pored surfaces; penetration behaviors of a water drop into a hydrophobic pore. Behaviors such as wettability, adhesion and penetration in water-solid interface of textured materials was studied through experimental and theoretical analysis approaches. In order to understand the physical interaction of a water drop on texture surfaces, hydrophobic polymer samples having micro/nano structures and vertically aligned pored structures were prepared. Hierarchical structure of micro-bead and nano-pore on textured surfaces were investigated to control wettability and adhesion of a drop. In textured surfaces, micro-beads were found to improve the hydrophobicity of textured surfaces, and nano-pores enhanced the adhesive force of a water drop. To design the textured materials, new wetting model and adhesion mechanism of textures surface were suggested.

Stability of a water drop on hydrophobic pores were studied based on the wettability by surface porosity and the net force of a drop. On a single pored sample and multiple pored samples, the critical conditions of pore size and drop volume were identified. They distinguishes a water drop being stable and being penetrative.

During penetration of a water drop into hydrophobic tube samples of varying inside and outside radii, the kinetic behaviors were examined. Two factors were identified affecting penetration: receding contact angle leads to a stick-slip-like motion of contact circle and the change of drop radius; the outside radius of a pored sample affects the penetration rate and trend. The maximum penetration was clearly identified.

Understanding the effects of geometrical factors on wettability, adhesion, and penetration is fundamentally important. This research revealed fundamental mechanisms of wettability, adhesion and penetration in water-solid interface of textured materials. Specific geometric design factors of textured materials were identified to control behaviors in water-solid interfaces. The findings in this research afford new approach to optimize applications of the textured surface.

6.2. Future recommendations

Based on the findings of this research, the following future works are recommended:

1) Kinetic study of uptake of a water drop into a hydrophobic capillary pore: this research focuses the penetration of a water drop having upward direction. A small drop has the spontaneous penetration into a hydrophobic pore considering capillary pressure. It can reveal the principle behind some phenomena such as capillary action of plants and imbibition of a water into porous materials. It will be helpful to design the micro/nano-fluidic devices having various directions.

2) Fabrication of hybrid porous materials: Penetration is related to wettability of a drop on porous surfaces as well as geometric factors such as pore size and drop volume.

Surface modification using physical method and chemical method is an easy way to control wettability. As shown in Wenzel's and Cassie-Baxter's models, surface roughness enhances their surface wetting. Hybrid materials having rough/textured surfaces and heterogeneous surface chemistry will have attractive penetration behaviors for many applications.

3) Investigation of the evaporation of a water drop in a capillary pore: Until now, this research has focused on wettability, adhesion and penetration. Beside these behaviors, penetrated water in a capillary pore shows interesting behaviors such as the change of meniscus angle and reducing penetration length. These behaviors are also related to the shape change of porous materials. It would be beneficial for extending the scope of this study in water-solid interfaces of textured materials.

REFERENCES

1. W. Adamson, A.P.G., *Physical Chemistry of Surface*. 6th ed. 1997, USA: Wiley-Interscience. 808.
2. Gaigeot, M.P. and M. Sulpizi, *Liquid–Solid Interfaces: Structure and Dynamics from Spectroscopy and Simulations.* Journal of Physics: Condensed Matter, 2014. 26(24): p. 240301.
3. Du, Q., E. Freysz, and Y.R. Shen, *Surface Vibrational Spectroscopic Studies of Hydrogen Bonding and Hydrophobicity.* Science, 1994. 264(5160): p. 826-828.
4. Zaera, F., *Probing Liquid/Solid Interfaces at the Molecular Level.* Chemical Reviews, 2012. 112(5): p. 2920-2986.
5. Hoffmann, M.R., et al., *Environmental Applications of Semiconductor Photocatalysis.* Chemical Reviews, 1995. 95(1): p. 69-96.
6. Koziel, S., et al., *International Conference On Computational Science, ICCS 2015Modeling Electrochemical Reactions at the Solid-liquid Interface Using Density Functional Calculations.* Procedia Computer Science, 2015. 51: p. 1887-1896.
7. Smart, R.S.C., *Mechanisms of Corrosion in Surface Layers at Solid-Solution Interfaces.* Ionics, 2001. 7(4): p. 275-289.
8. Al-Azizi, A.A., et al., *Effects of Nanoscale Surface Texture and Lubricant Molecular Structure on Boundary Lubrication in Liquid.* Langmuir, 2013. 29(44): p. 13419-13426.

9. Mante, P.-A., et al., *Probing Hydrophilic Interface of Solid/Liquid-Water by Nanoultrasonics.* Scientific Reports, 2014. 4: p. 6249.

10. Zaera, F., *Surface Chemistry at the Liquid/Solid Interface.* Surface Science, 2011. 605(13–14): p. 1141-1145.

11. Feng, L., et al., *Petal Effect: A Superhydrophobic State with High Adhesive Force.* Langmuir, 2008. 24(8): p. 4114-4119.

12. Ebert, D. and B. Bhushan, *Wear-Resistant Rose Petal-Effect Surfaces with Superhydrophobicity and High Droplet Adhesion using Hydrophobic and Hydrophilic Nanoparticles.* Journal of Colloid and Interface Science, 2012. 384(1): p. 182-188.

13. Ahn, H.S., et al., *Wicking and Spreading of Water Droplets on Nanotubes.* Langmuir, 2012. 28(5): p. 2614-2619.

14. Liu, M., et al., *Bioinspired Design of a Superoleophobic and Low Adhesive Water/Solid Interface.* Advanced Materials, 2009. 21(6): p. 665-669.

15. Latthe, S., et al., *Superhydrophobic Surfaces Developed by Mimicking Hierarchical Surface Morphology of Lotus Leaf.* Molecules, 2014. 19(4): p. 4256-4283.

16. Federle, W., et al., *Wet but not slippery: boundary friction in tree frog adhesive toe pads.* Journal of The Royal Society Interface, 2006. 3(10): p. 689-697.

17. Morrow, N.R., *Wettability and Its Effect on Oil Recovery.* Journal of Petroleum Technology, 1990. 42(12): p. 1476 - 1484.

18. Espinal, L., *Porosity and Its Measurement*, in *Characterization of Materials*. 2002, John Wiley & Sons, Inc.

19. Bixler, G.D. and B. Bhushan, *Fluid Drag Reduction with Shark-Skin Riblet Inspired Microstructured Surfaces.* Advanced Functional Materials, 2013. 23(36): p. 4507-4528.

20. Zhang, Y.-L., et al., *Recent Developments in Superhydrophobic Surfaces with Unique Structural and Functional Properties.* Soft Matter, 2012. 8(44): p. 11217-11231.

21. Ensikat, H.J., et al., *Superhydrophobicity in Perfection: the Outstanding Properties of the Lotus Leaf.* Beilstein Journal of Nanotechnology, 2011. 2: p. 152-161.

22. Su, Y., et al., *Nature's Design of Hierarchical Superhydrophobic Surfaces of a Water Strider for Low Adhesion and Low-Energy Dissipation.* Langmuir, 2010. 26(24): p. 18926-18937.

23. Ju, J., et al., *A Multi-Structural and Multi-Functional Integrated Fog Collection System in Cactus.* Nat Commun, 2012. 3: p. 1247.

24. Samuel, B., H. Zhao, and K.-Y. Law, *Study of Wetting and Adhesion Interactions between Water and Various Polymer and Superhydrophobic Surfaces.* The Journal of Physical Chemistry C, 2011. 115(30): p. 14852-14861.

25. Bhushan, B. and M. Nosonovsky, *The Rose Petal Effect and the Modes of Superhydrophobicity.* Philosophical Transactions of the Royal Society of London

A: Mathematical, Physical and Engineering Sciences, 2010. 368(1929): p. 4713-4728.

26. Teisala, H., M. Tuominen, and J. Kuusipalo, *Adhesion Mechanism of Water Droplets on Hierarchically Rough Superhydrophobic Rose Petal Surface.* Journal of Nanomaterials, 2011. 2011.

27. Schrader, M.E., *Young-Dupre Revisited.* Langmuir, 1995. 11(9): p. 3585-3589.

28. Lucas, R., *Ueber das Zeitgesetz des kapillaren Aufstiegs von Flüssigkeiten.* Kolloid-Zeitschrift, 1918. 23(1): p. 15-22.

29. Washburn, E.W., *The Dynamics of Capillary Flow.* Physical Review, 1921. 17(3): p. 273-283.

30. Berg, J.C., *An Introduction to Interfaces and Colloids: The Bridge to Nanoscience*. 2009, University of Washington, USA: World Scientific. 804.

31. Young, T., *An Essay on the Cohesion of Fluids.* Philosophical Transactions of the Royal Society of London, 1805. 95: p. 65-87.

32. Pierre-Gilles de Gennes, F.B.-W., David Quéré, *Capillarity and Wetting Phenomena. Drops, Bubbles, Pearls, Waves*. 2004, New York: Springer.

33. Latthe, S.S., et al., *Recent Progress in Preparation of Superhydrophobic Surfaces: A Review.* Journal of Surface Engineered Materials and Advanced Technology, 2012. 2(2): p. 76-94.

34. Wenzel, R.N., *Surface Roughness and Contact Angle.* The Journal of Physical and Colloid Chemistry, 1949. 53(9): p. 1466-1467.

35. Cassie, A.B.D. and S. Baxter, *Wettability of Porous Surfaces.* Transactions of the Faraday Society, 1944. 40(0): p. 546-551.

36. Furmidge, C.G.L., *Studies at Phase Interfaces. I. The Sliding of Liquid Drops on Solid Surfaces and a Theory for Spray Retention.* Journal of Colloid Science, 1962. 17(4).

37. Eral, H.B., D.J.C.M. 't Mannetje, and J.M. Oh, *Contact Angle Hysteresis: A Review of Fundamentals and Applications.* Colloid and Polymer Science, 2013. 291(2): p. 247-260.

38. Israelachvili, J.N., *Adhesion and Wetting Phenomena*, in *Intermolecular and Surface Forces (Third Edition)*, J.N. Israelachvili, Editor. 2011, Academic Press: San Diego. p. 415-467.

39. Bhushan, B. and Y. Chae Jung, *Wetting Study of Patterned Surfaces for Superhydrophobicity.* Ultramicroscopy, 2007. 107(10–11): p. 1033-1041.

40. Yang, S., et al., *Peanut Leaf Inspired Multifunctional Surfaces.* Small, 2014. 10(2): p. 294-299.

41. Marmur, A., *Penetration of a small drop into a capillary.* Journal of Colloid and Interface Science, 1988. 122(1): p. 209-219.

42. Schebarchov, D. and S.C. Hendy, *Dynamics of Capillary Absorption of Droplets by Carbon Nanotubes.* Physical Review E, 2008. 78(4): p. 046309.

43. Marmur, A., *Penetration and Displacement in Capillary Systems of Limited Size.* Advances in Colloid and Interface Science, 1992. 39: p. 13-33.

44. Lin, J., et al., *Fabrication of Biomimetic Superhydrophobic Surfaces Inspired by Lotus Leaf and Silver Ragwort Leaf.* Nanoscale, 2011. 3(3): p. 1258-1262.

45. Farhadi, S., M. Farzaneh, and S.A. Kulinich, *Anti-Icing Performance of Superhydrophobic Surfaces.* Applied Surface Science, 2011. 257(14): p. 6264-6269.

46. Zhang, X., et al., *Superhydrophobic Surfaces: from Structural Control to Functional Application.* Journal of Materials Chemistry, 2008. 18(6): p. 621-633.

47. Jung, Y.C. and B. Bhushan, *Mechanically Durable Carbon Nanotube−Composite Hierarchical Structures with Superhydrophobicity, Self-Cleaning, and Low-Drag.* ACS Nano, 2009. 3(12): p. 4155-4163.

48. Wenzel, R.N., *Resistance of Solid Surfaces to Wetting by Water.* Industrial & Engineering Chemistry, 1936. 28(8): p. 988-994.

49. Feng, L., et al., *Super-Hydrophobic Surfaces: From Natural to Artificial.* Advanced Materials, 2002. 14(24): p. 1857-1860.

50. Miwa, M., et al., *Effects of the Surface Roughness on Sliding Angles of Water Droplets on Superhydrophobic Surfaces.* Langmuir, 2000. 16(13): p. 5754-5760.

51. Öner, D. and T.J. McCarthy, *Ultrahydrophobic Surfaces. Effects of Topography Length Scales on Wettability.* Langmuir, 2000. 16(20): p. 7777-7782.

52. Ma, M., et al., *Superhydrophobic Fabrics Produced by Electrospinning and Chemical Vapor Deposition.* Macromolecules, 2005. 38(23): p. 9742-9748.

53. Burkarter, E., et al., *Superhydrophobic Electrosprayed PTFE.* Surface and Coatings Technology, 2007. 202(1): p. 194-198.

54. Yang, C., et al., *CF4 Plasma-modified Superhydrophobic PVDF Membranes for Direct Contact Membrane Distillation.* Journal of Membrane Science, 2014. 456: p. 155-161.

55. Latthe, S.S., et al., *Superhydrophobic Silica Films by Sol–Gel Co-Precursor Method.* Applied Surface Science, 2009. 256(1): p. 217-222.

56. Lau, K.K.S., et al., *Superhydrophobic Carbon Nanotube Forests.* Nano Letters, 2003. 3(12): p. 1701-1705.

57. S.T, A., et al., *Properties of Phase Separation Method Synthesized Superhydrophobic Polystyrene Films.* Applied Surface Science, 2012. 258(7): p. 3202-3207.

58. Feng, L., et al., *Creation of a Superhydrophobic Surface from an Amphiphilic Polymer.* Angewandte Chemie International Edition, 2003. 42(7): p. 800-802.

59. Jiang, L., Y. Zhao, and J. Zhai, *A Lotus-Leaf-like Superhydrophobic Surface: A Porous Microsphere/Nanofiber Composite Film Prepared by Electrohydrodynamics.* Angewandte Chemie International Edition, 2004. 43(33): p. 4338-4341.

60. Basu, B.B.J. and A.K. Paranthaman, *A Simple Method for the Preparation of Superhydrophobic PVDF–HMFS Hybrid Composite Coatings.* Applied Surface Science, 2009. 255(8): p. 4479-4483.

61. Amigoni, S., et al., *Covalent Layer-by-Layer Assembled Superhydrophobic Organic−Inorganic Hybrid Films.* Langmuir, 2009. 25(18): p. 11073-11077.

62. Park, S.H., et al., *Robust Superhydrophobic Mats based on Electrospun Crystalline Nanofibers Combined with a Silane Precursor.* ACS Applied Materials & Interfaces, 2010. 2(3): p. 658-662.

63. Yuyang, L., C. Xianqiong, and J.H. Xin, *Super-Hydrophobic Surfaces from a Simple Coating Method: a Bionic Nanoengineering Approach.* Nanotechnology, 2006. 17(13): p. 3259.

64. Jindasuwan, S., et al., *Surface Characteristics of Water-Repellent Polyelectrolyte Multilayer Films Containing Various Silica Contents.* Thin Solid Films, 2009. 517(17): p. 5001-5005.

65. Yan, L., K. Wang, and L. Ye, *Super Hydrophobic Property of PVDF/CaCO3 Nanocomposite Coatings.* Journal of Materials Science Letters, 2003. 22(23): p. 1713-1717.

66. Gu, X., et al., *Surface and Interfacial Properties of PVDF/Acrylic Copolymer Blends before and after UV Exposure.* Applied Surface Science, 2006. 252(14): p. 5168-5181.

67. Joo, J., et al., *Multigram Scale Synthesis and Characterization of Monodisperse Tetragonal Zirconia Nanocrystals.* Journal of the American Chemical Society, 2003. 125(21): p. 6553-6557.

68. Kaneko, Y. and T. Arake, *Sol-Gel Preparation of Highly Water-Dispersible Silsesquioxane/Zirconium Oxide Hybrid Nanoparticles.* International Journal of Polymer Science, 2012. 2012: p. 6.

69. Braga, F.J.C., et al., *Characterization of PVDF/HAP Composites for Medical Applications.* Materials Research, 2007. 10: p. 247-251.

70. Bottino, A., G. Capannelli, and A. Comite, *Preparation and Characterization of Novel Porous PVDF-ZrO2 Composite Membranes.* Desalination, 2002. 146(1–3): p. 35-40.

71. Bottino, A., et al., *The Formation of Microporous Polyvinylidene Difluoride Membranes by Phase Separation.* Journal of Membrane Science, 1991. 57(1): p. 1-20.

72. Deshmukh, S.P. and K. Li, *Effect of Ethanol Composition in Water Coagulation Bath on Morphology of PVDF Hollow Fibre Membranes.* Journal of Membrane Science, 1998. 150(1): p. 75-85.

73. Su, C., *A Simple and Cost-Effective Method for Fabricating Lotus-Effect Composite Coatings.* Journal of Coatings Technology and Research, 2012. 9(2): p. 135-141.

74. Lai, Y., et al., *Designing Superhydrophobic Porous Nanostructures with Tunable Water Adhesion.* Advanced Materials, 2009. 21(37): p. 3799-3803.

75. Guangming, G., et al., *A Novel Fluorinated Polyimide Surface with Petal Effect Produced by Electrospinning.* Soft Matter, 2014. 10(4): p. 549-552.

76. Pezron, I., G. Bourgain, and D. Quéré, *Imbibition of a Fabric.* Journal of Colloid and Interface Science, 1995. 173(2): p. 319-327.

77. Mulder, J., *Basic Principles of Membrane Technology*. 1996, Netherlands: Springer. 168.

78. Ng, T.W., et al., *Capillary Well Microplate.* Applied Physics Letters, 2008. 93(17): p. 174105.

79. Kettle, J., T. Lamminmäki, and P. Gane, *A Review of Modified Surfaces for High Speed Inkjet Coating.* Surface and Coatings Technology, 2010. 204(12–13): p. 2103-2109.

80. Morrow, N.R. and G. Mason, *Recovery of Oil by Spontaneous Imbibition.* Current Opinion in Colloid & Interface Science, 2001. 6(4): p. 321-337.

81. Günther, A. and M.T. Kreutzer, *Multiphase Flow,* in *Micro Process Engineering*. 2009, Wiley-VCH Verlag GmbH & Co. KGaA. p. 1-40.

82. Jongju, Y., et al., *Reverse Capillary Flow of Condensed Water through Aligned Multiwalled Carbon Nanotubes.* Nanotechnology, 2015. 26(23): p. 235701.

83. Yu, Y., X. Wang, and T.W. Ng, *Modeling the Liquid Filling in Capillary Well Microplates for Analyte Preconcentration.* Journal of Colloid and Interface Science, 2012. 376(1): p. 269-273.

84. Hilpert, M. and A. Ben-David, *Infiltration of Liquid Droplets into Porous Media: Effects of Dynamic Contact Angle and Contact Angle Hysteresis.* International Journal of Multiphase Flow, 2009. 35(3): p. 205-218.

85. Willmott, G.R., C. Neto, and S.C. Hendy, *Uptake of Water Droplets by Non-Wetting Capillaries.* Soft Matter, 2011. 7(6): p. 2357-2363.

86. Kim, S., A.A. Polycarpou, and H. Liang, *Electrical-Potential Induced Surface Wettability of Porous Metallic Nanostructures.* Applied Surface Science, 2015. 351: p. 460-465.

87. Choi, H., et al., *Design and Synthesis of a Superhydrophobic PVDF-Based Composite.* Journal of Tribology, 2015. 138(2): p. 022301-022301.

88. Hans-Jurgen Butt, K.G., Michael Kappl, *Physics and Chemistry of Interfaces*. Vol. 2nd Edition. 2006: Wiley-VCH. 9.

89. Yue, P. and Y. Renardy, *Spontaneous Penetration of a Non-Wetting Drop into an Exposed Pore.* Physics of Fluids, 2013. 25(5): p. 052104.

90. Kalová, J. and R. Mareš, *Reference Values of Surface Tension of Water.* International Journal of Thermophysics, 2015. 36(7): p. 1396-1404.

91. McDonald, J.C., et al., *Fabrication of Microfluidic Systems in Poly(dimethylsiloxane).* ELECTROPHORESIS, 2000. 21(1): p. 27-40.

92. Ruiz-Cabello, F.J.M., M.A. Rodriguez-Valverde, and M. Cabrerizo-Vilchez, *A New Method for Evaluating the Most Stable Contact Angle using Tilting Plate Experiments.* Soft Matter, 2011. 7(21): p. 10457-10461.

93. Ismail, A.E., et al., *Interfacial Structure and Dynamics of Siloxane Systems: PDMS−Vapor and PDMS−Water.* Macromolecules, 2009. 42(8): p. 3186-3194.

94. Hyväluoma, J., et al., *Simulation of Liquid Penetration in Paper.* Physical Review E, 2006. 73(3): p. 036705.

95. Kissa, E., *Wetting and Wicking.* Textile Research Journal, 1996. 66(10): p. 660-668.

96. Denesuk, M., et al., *Capillary Penetration of Liquid Droplets into Porous Materials.* Journal of Colloid and Interface Science, 1993. 158(1): p. 114-120.

97. Holman, R.K., et al., *Spreading and Infiltration of Inkjet-Printed Polymer Solution Droplets on a Porous Substrate.* Journal of Colloid and Interface Science, 2002. 249(2): p. 432-440.

98. Hapgood, K.P., et al., *Drop Penetration into Porous Powder Beds.* Journal of Colloid and Interface Science, 2002. 253(2): p. 353-366.

99. Flemming, M., L. Coriand, and A. Duparré, *Ultra-hydrophobicity Through Stochastic Surface Roughness.* Journal of Adhesion Science and Technology, 2009. 23(3): p. 381-400.

100. Marmur, A., *Soft Contact: Measurement and Interpretation of Contact Angles.* Soft Matter, 2006. 2(1): p. 12-17.

101. Zhao, Y., *Moving Contact Line Problem: Advances and Perspectives.* Theoretical and Applied Mechanics Letters, 2014. 4(3): p. Article 034002.

102. E B Dussan, V., *On the Spreading of Liquids on Solid Surfaces: Static and Dynamic Contact Lines.* Annual Review of Fluid Mechanics, 1979. 11(1): p. 371-400.

103. Wang, F. and H. Wu, *Molecular Origin of Contact Line Stick-Slip Motion during Droplet Evaporation.* Scientific Reports, 2015. 5: p. 17521.

104. Xu, W. and C.-H. Choi, *From Sticky to Slippery Droplets: Dynamics of Contact Line Depinning on Superhydrophobic Surfaces.* Physical Review Letters, 2012. 109(2): p. 024504.

105. Choi, H. and H. Liang, *Wettability and Spontaneous Penetration of a Water Drop into Hydrophobic Pores.* Journal of Colloid and Interface Science, 2016. 477: p. 176-180.

106. Morra, M., et al., *On the Aging of Oxygen Plasma-Treated Polydimethylsiloxane Surfaces.* Journal of Colloid and Interface Science, 1990. 137(1): p. 11-24.

107. Spori, D.M., *Structural Influences on Self-cleaning Surfaces*, in *Material Science*. 2010, ETH Zurich: Switzerland. p. 180.

108. Martic, G., et al., *A Molecular Dynamics Simulation of Capillary Imbibition.* Langmuir, 2002. 18(21): p. 7971-7976.

APPENDIX A

CHAPTER III SUPPLEMENTARY DATA

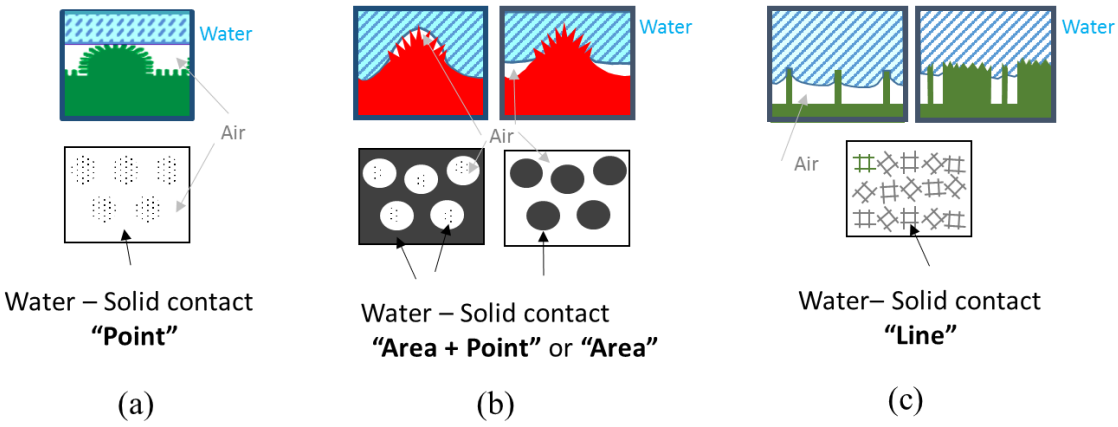

Figure A.1 Schematics of water-solid interfaces of (a) lotus leaf, (b) rose petal and (c) peanut leaf in micro-scale

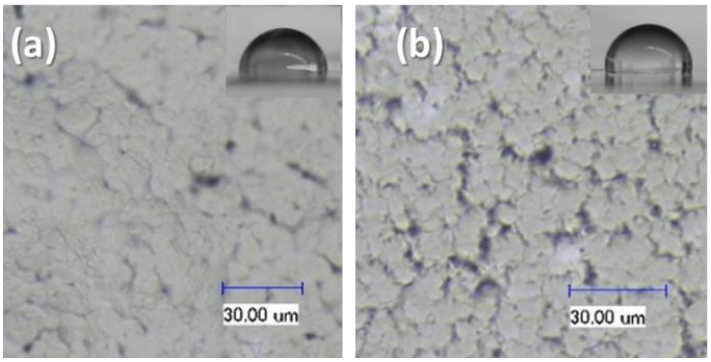

Figure A.2 Optical micrographs of PVDF films fabricated (a) on glass slide and (b) on hot glass slide (150 °C). When prepared PVDF solution was sprayed on glass slides, it formed flat spherical shapes due to collision by air flow. The evaporation of PVDF solution was slow, accumulated droplets lost their shapes because sprayed droplets were dissolved by remaining DMSO.

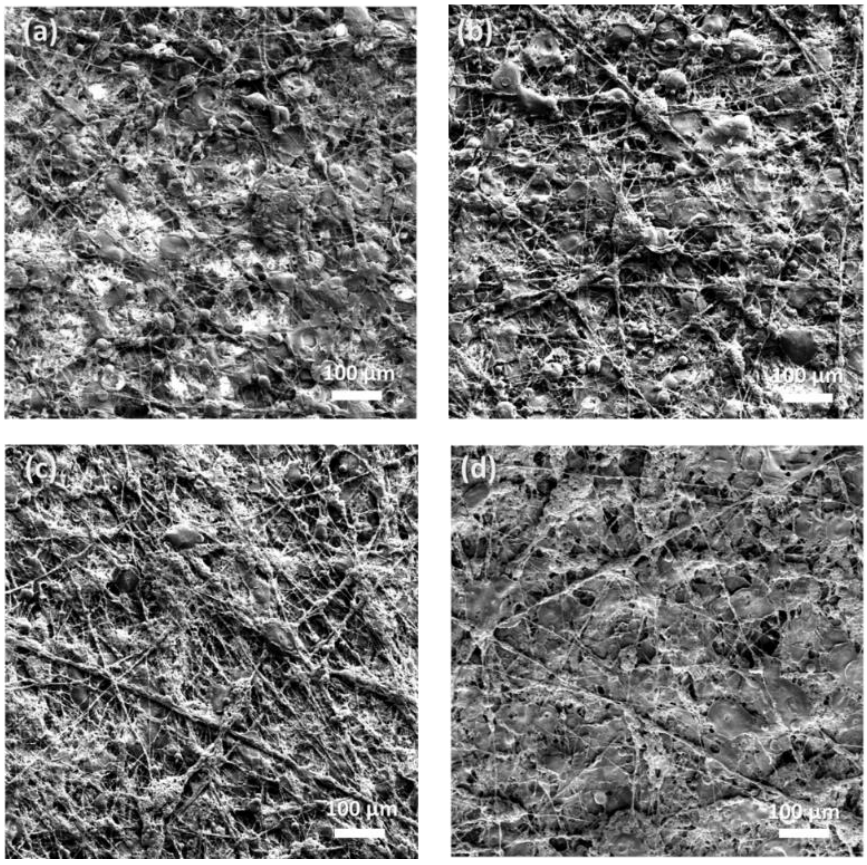

Figure A.3 SEM images of upper sides: PVDF film (a) on water, (b) on ethanol/water and PVDF/ZrO_2 composite film (c) on water, (d) on ethanol/water

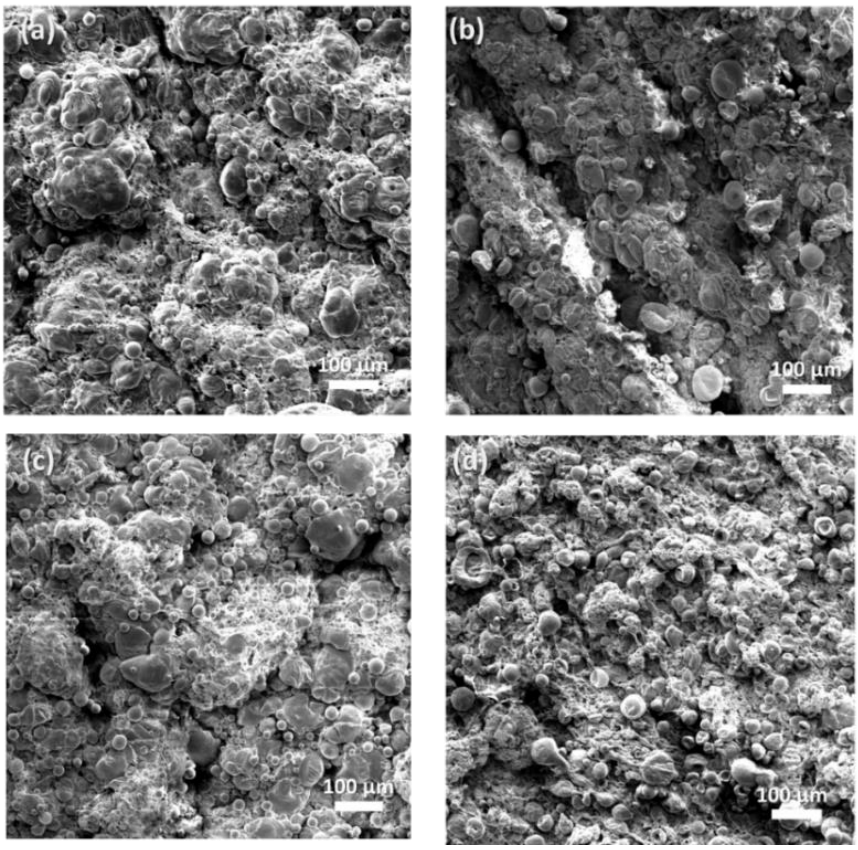

Figure A.4 SEM images of bottom sides: PVDF film (a) on water, (b) on ethanol/water and PVDF/ZrO_2 composite film (c) on water, (d) on ethanol/water

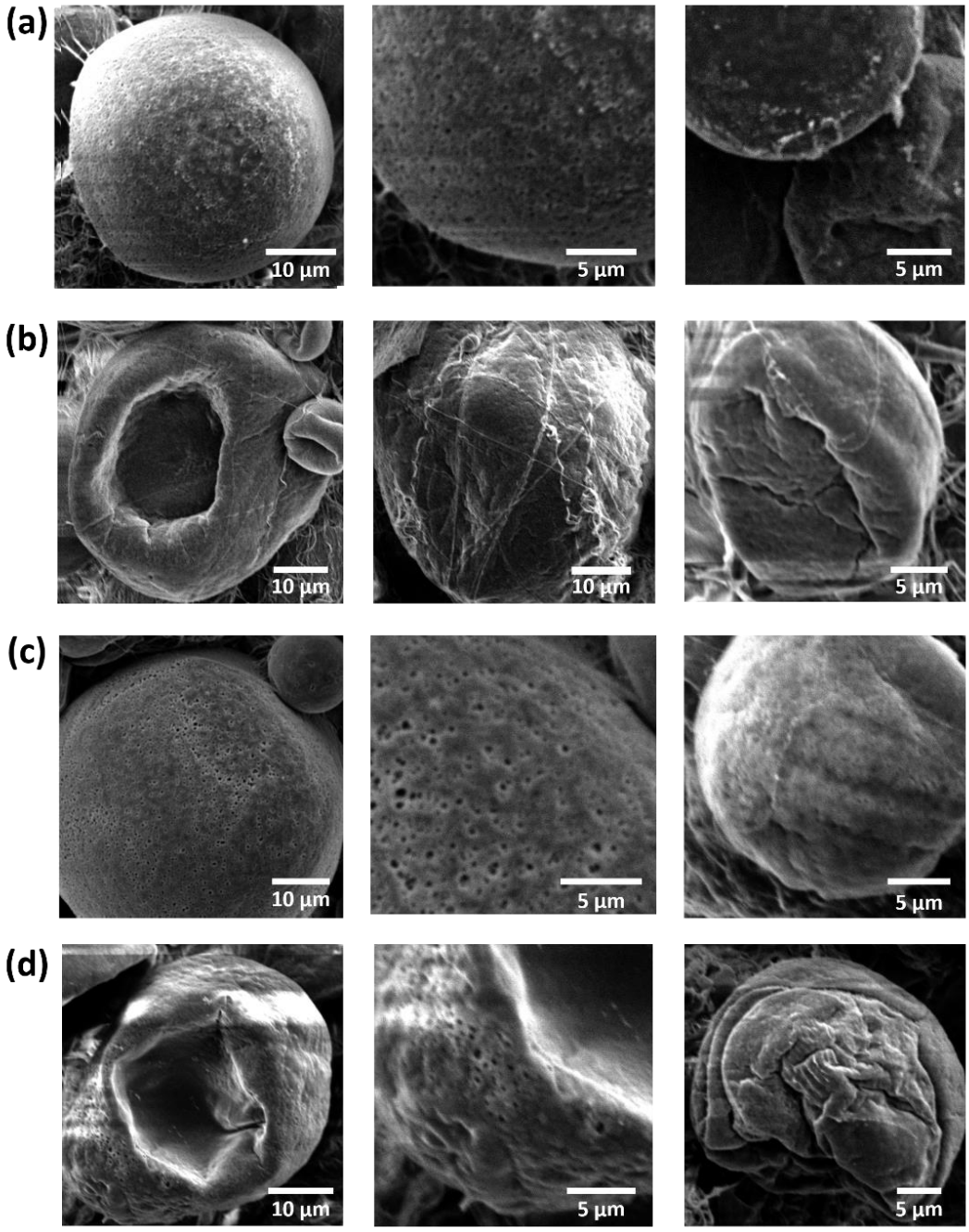

Figure A.5 SEM images of beads on bottom: PVDF film (a) on water, (b) on ethanol/water and PVDF/ZrO_2 composite film (c) on water, (d) on ethanol/water

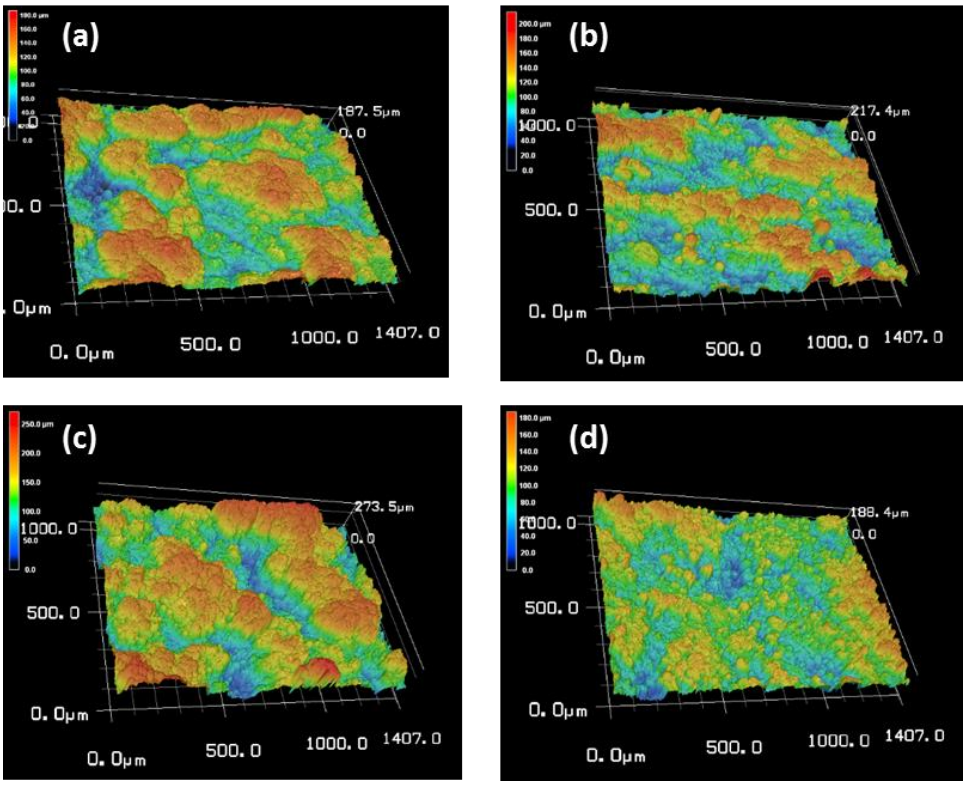

Figure A.6 Roughness of bottom sides: PVDF film (a) on water, (b) on ethanol/water and PVDF/ZrO_2 composite film (c) on water, (d) on ethanol/water

APPENDIX B

CHAPTER IV SUPPLEMENTARY DATA

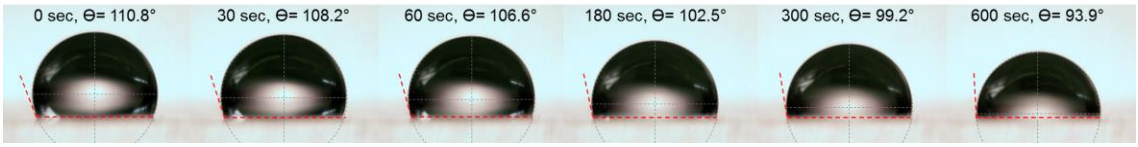

Figure B.1 Short-term observation of wetting angle of a water drop (3 µL) on PDMS flat surface

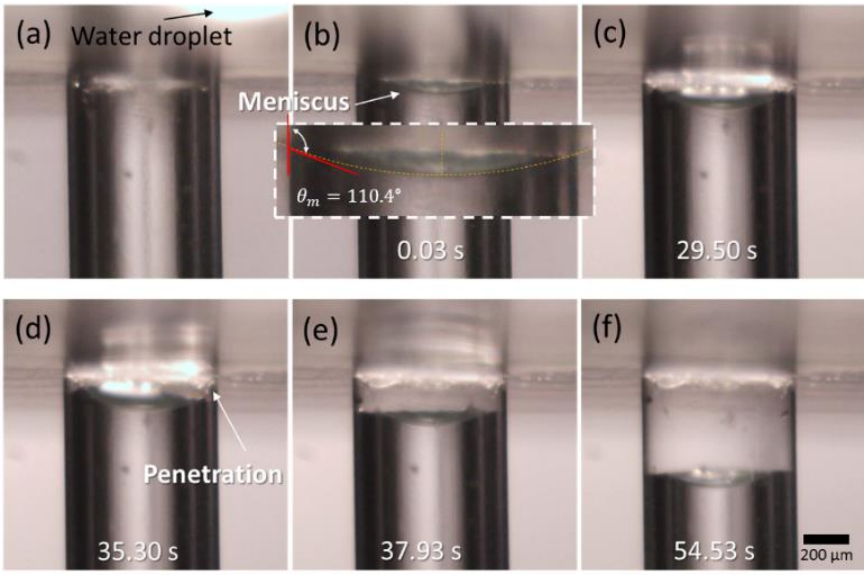

Figure B.2 Penetration process of a water drop (3.2 µL) into PDMS straight-edged pore. Meniscus angle was observed as (b) before penetration.

As shown in Figure B.3, to determine the penetration of a water drop on a single pore, three forces are considered in initial static state: force by Laplace pressure, gravitational force of a drop and capillary force (or surface tension force) by a meniscus in a pore. Laplace pressure is calculated by

$$F_D = \Delta p \frac{\pi d^2}{4} = \left(\frac{2\gamma}{R_d}\right)\frac{\pi d^2}{4}$$

Gravitational force of a drop is calculated by

$$F_G = \rho g h \frac{\pi d^2}{4} = \rho g R_d (1-\cos\theta)\frac{\pi d^2}{4}$$

Capillary force (or surface tension force) by a meniscus in a pore is calculated by

$$F_M = \left(\frac{2\gamma}{R_m}\right)\frac{\pi d^2}{4} = \left(\frac{4\gamma\cos(\pi-\theta_m)}{d}\right)\frac{\pi d^2}{4} = \pi d\gamma\cos(\pi-\theta_m)$$

For penetration into a pore: the net force is like $F_{Net} = F_L + F_G - F_M > 0.$

$$F_{Net}^S = \frac{\pi\gamma d^2}{2R_d} + \rho g R_d (1-\cos\theta)\frac{\pi d^2}{4} - \pi d\gamma\cos(\pi-\theta_m) > 0$$

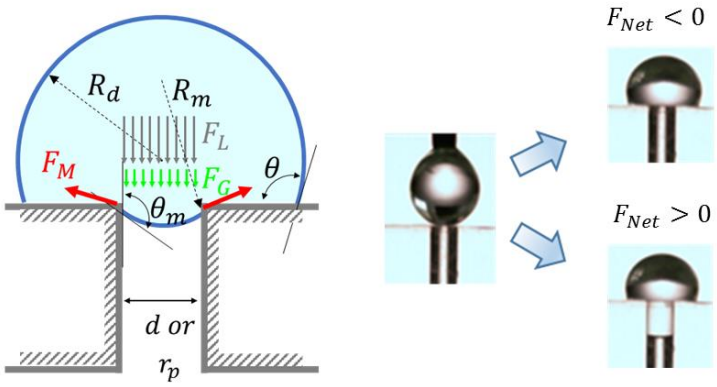

Figure B.3 Schematic of a water drop on a single-pored sample for spontaneous penetration.

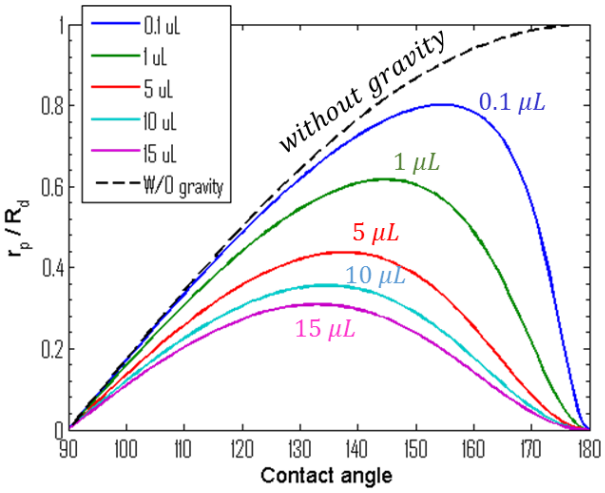

Figure B.4 Equilibrium ratio of a pore radius (r_p) and a droplet radius (R_d) vs. CA (°). This ratio without gravity is dependent on CA regardless of the droplet volume (or size).

Ignoring gravity, the ratio follows this relation as $\frac{r_p}{R_d} > \cos(\pi - \theta_Y)$. Considering gravity, this ratio has this relation,

$$r_p \left[\frac{\pi \rho g}{6\gamma} \frac{(2 - 3\cos\theta_Y + \cos^3\theta_Y)}{\sin^2(\pi - \theta_Y)} R_d + \frac{1}{R_d} \right] \geq \cos(\pi - \theta_Y).$$

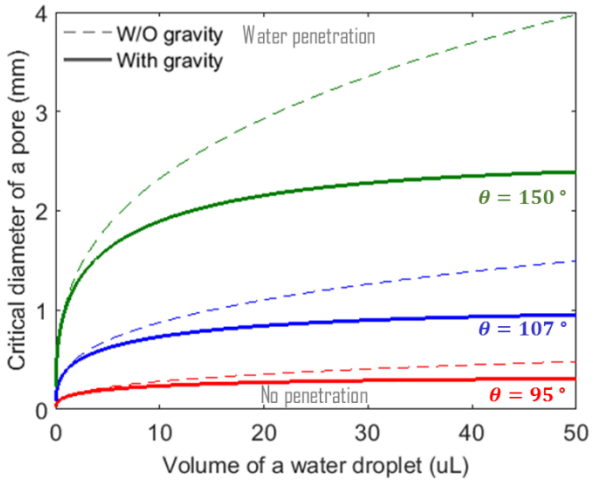

Figure B.5 Critical diameter of a pore is the minimum diameter for penetration. Critical volume is the maximum volume of a drop for penetration.

Critical diameter of a pore

$$d > d_{\min} = \cos(\pi - \theta_Y) / \left[\frac{2}{R_d} + \frac{\rho g R_d (1 - \cos\theta_Y)}{\gamma} \right]$$

Critical volume of a drop

$$V < V_{\max} = \Theta^3 \left[\frac{-\cos\theta_Y \pm \sqrt{\cos^2\theta_Y - 8d^2 G}}{2dG} \right]^3$$

$$R_d < R_{d\max} = \left[\frac{-\cos\theta_Y \pm \sqrt{\cos^2\theta_Y - 8d^2 G}}{2dG} \right]$$

$$G = \frac{\rho g (1 - \cos\theta_Y)}{\gamma}, \quad \Theta(\theta_Y) = \frac{\pi}{3}(2 - 3\cos\theta_Y + \cos^3\theta_Y)$$

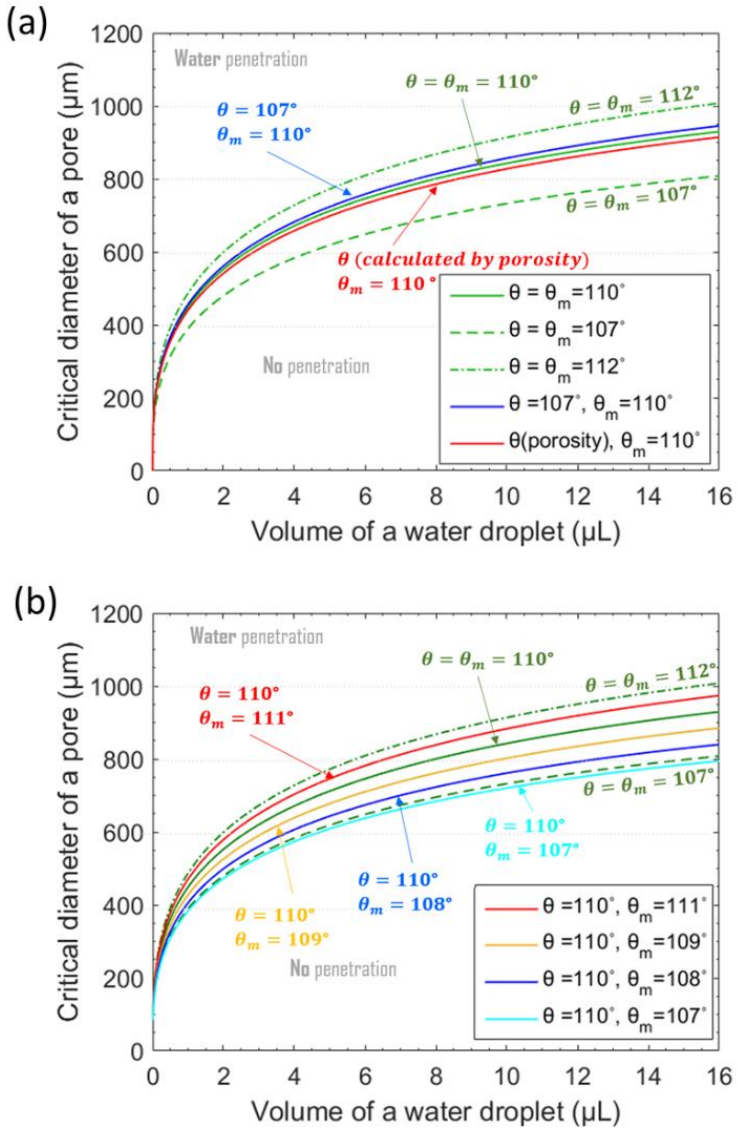

Figure B.6 Sensitivity analysis about the critical condition between pore size and drop volume by water contact angle and meniscus angle

Wetting angle by Cassie-Baxter's model

Calculation of wetting angle on a single pore by Cassie-Baxter's model.

$$R_d = \sqrt[3]{\frac{3V_d}{\pi(2-3\cos\theta_Y+\cos^3\theta_Y)}}$$

Contact area of a drop on surface $\approx R_d \sin(\pi-\theta_f)$

$$f_{S-L}^S = 1-\frac{\pi {r_p}^2}{\pi {R_d}^2 \sin^2\theta_Y},\ f_{A-L}^S = \frac{\pi {r_p}^2}{\pi {R_d}^2 \sin^2\theta_Y}$$

$$\cos\theta_{CB}{}^S = f_{S-L}^S \cos\theta_Y - f_{A-L}^S$$

Calculation of wetting angle on multiple pores by Cassie-Baxter's model.

$$R_d = \sqrt[3]{\frac{3V_d}{\pi(2-3\cos\theta_Y+\cos^3\theta_Y)}}$$

Contact area of a drop on surface $\approx R_d \sin(\pi-\theta_Y)$

If there are ordered pores (Fig. 1b), $n = \frac{2}{\sqrt{3}p^2}$, $N = n{R_d}^2 \sin^2\theta_Y$

$$f_{S-L}^M = 1-N\frac{\pi {r_p}^2}{\pi {R_d}^2 \sin^2\theta_Y},\ f_{A-L}^M = N\frac{\pi {r_p}^2}{\pi {R_d}^2 \sin^2\theta_Y}$$

$$\cos\theta_{CB}{}^M = f_{S-L}^M \cos\theta_Y - f_{A-L}^M$$

APPENDIX C

CHAPTER VI SUPPLEMENTARY DATA

The initial contact angle and the initial radius of a drop on tube-like pored sample can be predicted based on volume conservation and geometrical consideration by the following equations.

When $r_t > R_{C0}$,

$$R_{d0} = \left[\frac{3V_0}{\left(2 - 3\cos\theta_{d0} + \cos^3\theta_{d0}\right)} \right]^{1/3}, \quad \theta_{d0} \approx \theta_0 \text{ (YCA)}$$

$$R_{d0} = R_{c0} / \sin\theta_{d0}$$

When $r_p < r_t < R_{C0}$,

$$R'_d = R'_{c0} / \sin\theta'_{d0}, \quad R'_{c0} = r_t, \quad \theta'_{d0} > \theta_{d0}$$

$$R'_d = \left[\frac{3V_0}{\pi\left(2 - 3\cos\theta'_{d0} + \cos^3\theta'_{d0}\right)} \right]^{1/3}$$

$$\Rightarrow \frac{\pi r_t^3}{3V_0} = \frac{\sin^3\theta'_d}{\left(2 - 3\cos\theta'_{d0} + \cos^3\theta'_{d0}\right)}$$

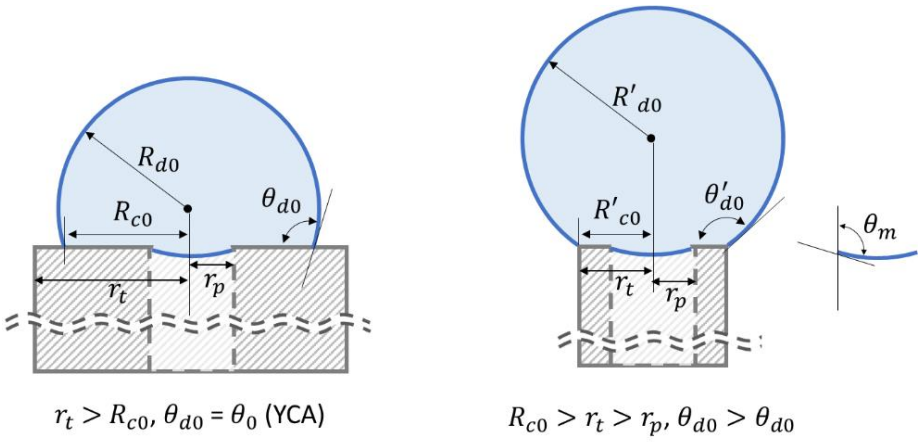

Figure C.1 Schematics of capillary systems with different outside radii

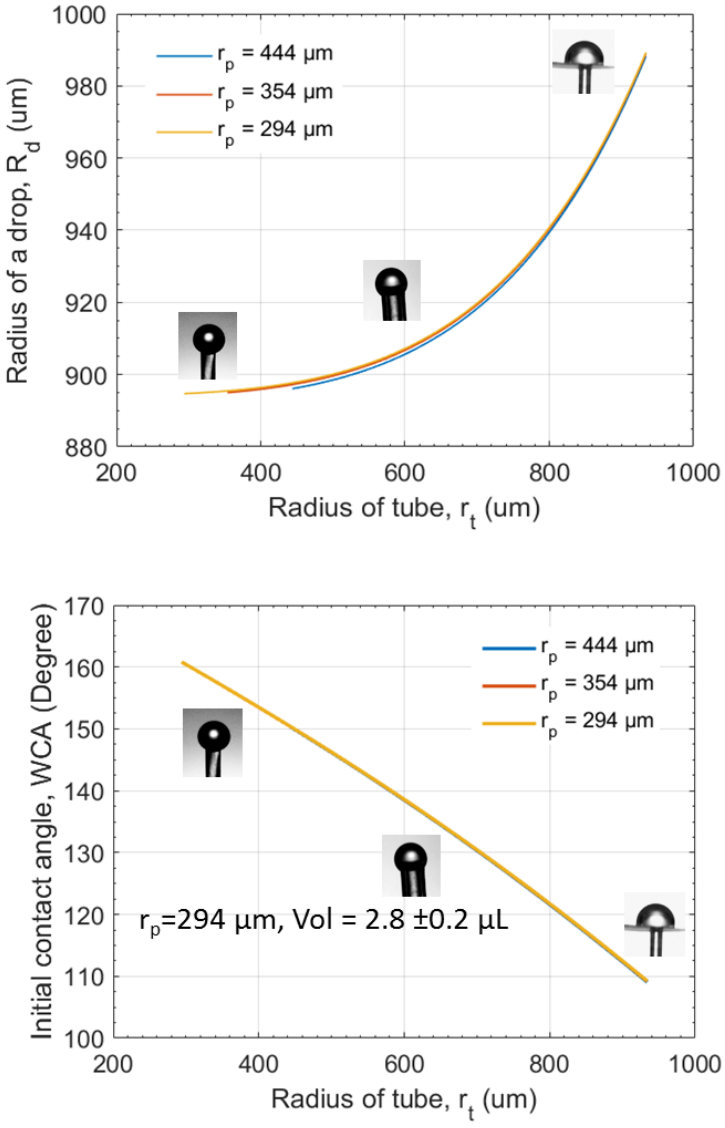

Figure C.2 The relation between the outside radius of a tube and the initial contact angle based on the geometric consideration. Pictures on plots shows initial water drops on different tubes. Pore radius (r_p) is 294 µm and drop volume is 2.8 ± 0.2 µL.